

Human lung conventional dendritic cells orchestrate lymphoid neogenesis during COPD

Authors: Thomas Naessens¹, Yannick Morias^{2*}, Eva Hamrud^{1*}, Ulf Gehrman¹, Ramachandramouli Budida¹, Johan Mattsson¹, Tina Baker³, Gabriel Skogberg⁴, Elisabeth Israelsson¹, Kristofer Thörn¹, Martijn J. Schuijs⁵, Bastian Angermann¹, Faye Melville⁶, Karl J Staples⁶, Danen M Cunoosamy^{1#}, Bart N Lambrecht^{7,8,9#}

Affiliations

¹Translational Science and Experimental Medicine, Research and Early Development, Respiratory, Inflammation, Autoimmunity, BioPharmaceuticals R&D, AstraZeneca, Gothenburg, Sweden

²Bioscience Cardiovascular, Research and Early Development, Cardiovascular, Renal and Metabolism (CVRM), BioPharmaceuticals R&D, AstraZeneca, Gothenburg, Sweden

³Translational Science and Experimental Medicine, Research and Early Development, Respiratory, Inflammation, Autoimmunity, BioPharmaceuticals R&D, AstraZeneca, Cambridge, UK

⁴Bioscience COPD/IPF, Research and Early Development, Respiratory, Inflammation, Autoimmunity, BioPharmaceuticals R&D, AstraZeneca, Gothenburg, Sweden

⁵Cancer Research UK Cambridge Institute, University of Cambridge, Cambridge, UK

⁶University of Southampton, Faculty of medicine, Clinical and Experimental Sciences, Southampton, United Kingdom of Great Britain and Northern Ireland

⁷Laboratory of Immunoregulation, VIB-UGhent Center for Inflammation Research, Ghent, Belgium

⁸Department of Internal Medicine and Pediatrics, Ghent University, Ghent, Belgium

26 ⁹Department of Pulmonary Medicine, Erasmus University Medical Center, Rotterdam, The
27 Netherlands

28

29 *Yannick Morias and Eva Hamrud contributed equally to this paper

30 #Danen Cunoosamy and Bart Lambrecht co-supervised the study

31

32 All correspondence to Thomas Naessens: Pepparedsleden 1, 431 50 Mölndal (Gothenburg),
33 Sweden; Thomas.Naessens@AstraZeneca.com

34

35 M.J.S. was supported by an EMBO long-term post-doctoral fellowship (ALTF 423-2017)

36

37 Author contributions: T.N., K.J.S., D.M.C., and B.N.L. designed experiments, T.N., Y.M.,
38 E.H., U.G., J.M., R.B., M.J.S., G.S., K.T. and F.A. performed experiments. T.N., E.H., U.G.,
39 T.B., E.I. and B.A. analyzed data. T.N., D.M.C, and B.N.L. wrote the manuscript with input
40 from all co-authors.

41

42 Running head: Lung cDC2 drive lymphoid neogenesis during COPD.

43

44 Descriptor number: 9.13 COPD: Pathogenesis

45

46 Total word count: 4136

47

48

49 **At a Glance Commentary**

50

51 Scientific Knowledge of on the Subject

52 Chronic obstructive pulmonary disease (COPD) severity and tissue destruction correlate with
53 the development of tertiary lymphoid organs (TLO). T follicular helper (Tfh)-cells represent a
54 specialized CD4⁺ T-cell subset, key for lymphoid organ formation. Dendritic cells (DC) are
55 potent inducers of CD4⁺ T-cell responses, including Tfh-cell responses. However, how human
56 lung DC polarize Tfh-cells during COPD and hence contribute to the generation of TLOs
57 remains to be elucidated.

58

59 What this Study Adds to the Field

60 Single cell RNA sequencing showed that the myeloid cell compartment in the human non-
61 obstructed lung is highly heterogeneous, containing multiple DC and monocyte/macrophage
62 subsets. Among these, CD1c⁺ conventional (c)DC (cDC2) were the most potent inducers of
63 Tfh-cell polarization. Importantly, compared to cDC2 from non-obstructed control lungs, cDC2
64 derived from COPD lungs showed increased potential to polarize Tfh-cells. Mechanistically,
65 cDC2 exhibited a unique migratory signature, including expression of the oxysterol receptor
66 EBI2, known to control spatial organization of immune cells in TLO. Furthermore, we
67 demonstrated the crucial contribution of the OX40-OX40L co-stimulatory axis to cDC2
68 mediated Tfh-cell induction. Additionally, cDC2 exhibited (transcriptional) expression of
69 several other pathways and genes related to DC-induced Tfh-priming. Together, our study
70 revealed a novel immune mechanism underlying TLO formation during COPD pathogenesis.

71

72

73

74 Impact: Our study reveals a new (immune) mechanism underlying TLO formation during
75 COPD and argues for increased investigation of the role of this pathway, and TLO formation
76 in general, in COPD pathogenesis and progression. In addition, the data provide conceptual
77 advances regarding the formation of TLO during other respiratory and non-respiratory diseases
78 and contribute to the field of human lung dendritic cells and T follicular helper cells.

79 **Abstract**

80 **Rationale:** Emerging evidence supports a crucial role for tertiary lymphoid organs (TLOs) in
81 chronic obstructive pulmonary disease (COPD) progression. However, mechanisms of immune
82 cell activation leading to TLO in COPD remain to be defined.

83 **Objectives:** To examine the role of lung dendritic cells (DC) in T follicular helper (Tfh)-cell
84 induction, a T-cell subset critically implicated in lymphoid organ formation, in COPD.

85 **Methods:** Myeloid cell heterogeneity and phenotype was studied in an unbiased manner via
86 single-cell RNA sequencing on HLA-DR⁺ cells sorted from human lungs. The *in vitro*
87 capability of FACS-sorted DC-subsets of control and COPD lungs to polarize IL-21⁺CXCL13⁺
88 Tfh-like cells was measured. *In situ* imaging analysis was performed on COPD stage IV GOLD
89 lungs with TLO.

90 **Measurements and Main Results:** ScRNAseq analysis revealed a high level of heterogeneity
91 among human lung myeloid cells. Among these, cDC2 showed increased induction of IL-
92 21⁺CXCL13⁺ Tfh-like cells. Importantly, the capacity to induce IL-21⁺ Tfh-like cells was
93 higher in cDC2s from COPD patients compared with control patients. Increased Tfh-induction
94 by COPD cDC2 correlated with increased presence of Tfh-like cells in COPD lungs as
95 compared to controls, and cDC2 co-localized with Tfh-like cells in TLOs of COPD.
96 Mechanistically, cDC2 exhibited a unique migratory signature and (transcriptional) expression
97 of several pathways and genes related to DC-induced Tfh-priming. Importantly, blocking the
98 co-stimulatory OX40L-OX40 axis reduced Tfh-induction by control lung cDC2.

99 **Conclusions:** In COPD lung, we found lung EB12⁺ OX-40L-expressing cDC2 that induces IL-
100 21⁺ Tfh-like cells, suggesting an involvement of these cells in TLO formation.

101 Abstract word count: 247

102

103 **Introduction**

104 Chronic obstructive pulmonary disease (COPD) is currently the third leading
105 cause of death worldwide (1) and is characterized by progressive airway inflammation,
106 emphysema and impaired lung function resulting from inhaled oxidants such as cigarette smoke
107 (CS). COPD severity and tissue destruction correlate with development of tertiary lymphoid
108 organs (TLO) (2, 3). While rarely developing in healthy individuals, lung TLO formation is
109 significantly increased in COPD (GOLDI/II) patients (4). Finally, in severe/end-stage COPD
110 patients (GOLD III/IV), TLO numbers and size further increase and can be found in nearly 50%
111 of the small airways (2, 4). TLOs consist of well-defined B-cell follicles surrounded by T-cells
112 interspersed with dendritic cells (DC), reminiscent of the structural organization also seen in
113 secondary lymphoid organs (5). Several studies have shown that absence of TLOs via either
114 use of B-cell deficient mice (6) or antibodies blocking B-cell recruitment (7) or survival (4, 8),
115 prevented CS-induced emphysema in a murine COPD model. However, mechanisms governing
116 TLO formation during COPD remain to be elucidated.

117 Peripheral T follicular helper (Tfh-)like cells exhibit phenotypic overlap with
118 ‘bona fida’ Tfh-cells and regulate local B-cell isotype switching in peripheral diseased organs,
119 including skin (9), synovial tissue (10) and lung (11) via IL-21 secretion. Importantly, we and
120 others have also described the presence of IL-21⁺ Tfh-like cells in TLO of idiopathic pulmonary
121 arterial hypertension (IPAH) (12) and COPD (3) lungs, suggesting these cells are involved in
122 TLO formation and maintenance.

123 Human DC are heterogeneous and consists of different subsets, including two
124 conventional (c)DC populations (CD141⁺ cDC1 and the CD1c⁺ cDC2) and plasmacytoid (p)DC
125 (13, 14). It has been shown that mice, in which DC were depleted, failed to develop and
126 maintain lung TLO in response to allergens or virus infection (15-17). In contrast, repeated
127 pulmonary delivery of activated DC was sufficient to induce TLO formation (15, 18). These

128 studies highlight a crucial role for DC in TLO formation and maintenance. However, how DC
129 induce TLO, especially during COPD, is unknown.

130 We hypothesized that human lung DC induce Tfh-like cell polarization and hence
131 contribute to subsequent lymphoid neogenesis during COPD. We first used an unbiased
132 approach to address the complexity of Lineage(Lin)⁻HLA-DR⁺ lung cells and found a high level
133 of heterogeneity. We then demonstrated that cDC2 are the most efficient subset in inducing IL-
134 21⁺ Tfh-like cells. Importantly, cDC2 isolated from COPD lungs showed increased potential to
135 polarize Tfh-like cells. Mechanistically, we found that cDC2 expressed a unique migratory
136 signature, suggesting these cells are highly capable to migrate to the site of TLO formation and
137 subsequently interact with CD4⁺ T-cells. Furthermore, blocking the co-stimulatory OX40L-
138 OX40 axis reduced Tfh-induction by cDC2 derived from non-obstructed control lungs. Some
139 of the results have been previously reported in the form of an abstract (19).

140 **Methods**

141 Detailed description of materials and methods can be found in the online methods supplement.

142

143 ***Human lung samples***

144 Lung samples were obtained from non-obstructed control or COPD subjects. Study and consent
145 procedures were reviewed and approved by the Swedish Research Ethical Committee in
146 Gothenburg, Sweden (FEK 675-12/2012 and 1026-15, March 2016) in accordance with the
147 principles of the Declaration of Helsinki. Written informed consent was obtained
148 preoperatively. Table 1 shows demographics and lung function. Additional information about
149 the source and processing of the human lung tissue samples is described in the online methods
150 supplement.

151

152 ***In vitro DC/T-cell co-cultures***

153 Mixed Leukocyte Reactions (MLR) were set up between FACS-sorted lung DC populations
154 and allogeneic naïve blood CD4⁺ T-cells as described in the online supplement. T-cell
155 proliferation and polarization, including cytokine and transcription factor profiling, were
156 subsequently analyzed via flow cytometry as described in the online supplement.

157

158 ***Ex vivo phenotyping of lung leukocyte populations***

159 Flow cytometry was used to assess expression of extracellular and intracellular phenotypic
160 protein markers by lung DC and T-cell subsets as described in the online supplement. Single-
161 cell RNA transcriptomes of the lung HLA-DR⁺ fraction were generated and analyzed as
162 described in the online supplement.

163

164

165 ***In situ imaging of GOLD IV COPD lung TLO***

166 To image *CH25H* and *CD19* mRNA topography in the lung TLO, RNAScope was performed
167 as described in the online supplement. Fluorescence microscopy was used to determine the
168 presence and anatomical localization of cDC2 in lung TLO as described in the online
169 supplement.

170 **Results**

171 **Unbiased single cell RNA sequencing analysis of human lung Lin⁻HLA-DR⁺ cells.**

172 Myeloid cells represent a heterogeneous population and comprise several
173 subtypes (14). To date, definition of human lung myeloid cells was biased by the limited
174 markers available to identify and isolate the cells. To identify the different myeloid cell
175 populations in the human lung in an unbiased way, we performed single-cell RNA sequencing
176 on Lin⁻HLA-DR⁺ cells from non-obstructed lungs. Different DC (including cDC1, cDC2 and
177 pDC) and monocyte subsets (including CD14⁺, CD16⁺ and CD14⁺CD16⁺ monocytes) were
178 FACS-sorted based on the expression of DC and monocyte subset defining surface markers
179 (Figure E1A) (14) and pooled afterwards in enriched proportions before sequencing.

180 Unsupervised clustering identified 14 clusters (Figure 1A). Differential gene
181 expression between clusters was analyzed (Figure 1B). Cluster 1 highly expressed cDC2-
182 associated genes such as *CD1C*, *CLEC10A*, *FCERIA* and *CD1A*. Cluster 2 highly expressed
183 monocyte/macrophage-related genes such as *MRC1*, *CTSD*, *MARCO* and *VSIG4* while cluster
184 3 is characterized by cell cycle gene expression, including *TOP2A*, *CENPF1* and *STMN1*.
185 Cluster 4 expressed high levels of pDC-associated genes, including *TCF4*, *GZMB*, *CLEC4C*
186 and *BCL11A* while cluster 5 exhibited high expression levels of monocyte/macrophage-related
187 genes, including *S100A8*, *S100A9*, *FCN1* and *VCAN*. Cluster 6 expressed natural killer (NK)
188 cell-associated genes, like *GZMA*, *CD96* and *GPLY* while cluster 7 displayed expression of
189 monocyte/macrophage-related genes, including *FCGR3A*, *CTSS*, *PECAM1* and *MAFB*. Cluster
190 8 expressed high levels of cDC1 genes, including *CLEC9A*, *IRF8*, *ID2* and *XCRI*. Cluster 9
191 exhibited expression of type II alveolar epithelial cells (AEC), including *SFTPC*, *SFTPB*,
192 *SFTPD* and *EPCAM*. Cluster 10 expressed endothelial cell-related genes including *VWF*, *CAVI*
193 and *GIMAP7*. Furthermore, both cluster 9 and cluster 10 lack expression of the pan-leukocyte
194 marker gene *PTPRC* (coding for CD45), further confirming their non-immune cell nature

195 (Figure E1B). Cluster 11 highly expressed genes associated with DC activation, including
196 *CCR7*, *CCL22*, *LAMP3* and *BIRC3*. Both cluster 12 and cluster 14 expressed
197 monocyte/macrophage-related genes, like *CXCL10*, *CXCL11*, *CCL8* and *GBP1* for cluster 12
198 and *LYVE1*, *CIQA*, *CD163* and *CD14* for cluster 14. Finally, cluster 13 exhibited expression of
199 mast cell genes, including *KIT*, *CPA3* and *MS4A2*. The complete list of top 20 differentially
200 expressed genes is available in Table S1.

201 To confirm the identity of the different clusters, we calculated signature scores
202 for each single cell using published transcriptome signatures for human blood (20) and lung
203 (21) leukocyte subsets (Figure 1C). Cluster 1 had the highest score for the cDC2 signature while
204 cluster 2 exhibited score increase for CD14⁺⁺CD16⁺ monocyte and CD14⁺ and CD16⁺ monocyte
205 cell signatures. Cluster 3 showed an overlap with a signature defining a proliferating
206 monocyte/macrophage (Mac/mono cycl.) subset as observed in (21). Cluster 4 displayed a clear
207 overlap with the pDC signature while cluster 5 exhibited a high score for the CD14⁺ monocyte
208 and CD14⁺CD16⁺ monocyte signature. Cluster 6 overlapped with the NK cell signature and
209 cluster 7 with the CD16⁺ monocyte and CD14⁺⁺CD16⁺ monocyte cell signature. Cluster 8
210 showed a clear overlap with the cDC1 signature while cluster 9 and cluster 10 overlapped with
211 signatures of type II AEC and endothelial cells respectively. For cluster 11, we observed a high
212 overlap with an ‘activated DC’ signature. As expected, both cluster 12 and cluster 14 had high
213 signature scores for macrophage phenotypes (mac1 and mac2 respectively) observed earlier in
214 the lung (21). Finally, cluster 13 had a high score for a mast cell signature.

215 Based on the relevance in terms of their potency to prime T-cell activation and
216 polarization we opted to primarily focus on cDC2, cDC1 and pDC, rather than on macrophage
217 subsets, NK-cells, mast cells and structural cells for the rest of the study. All monocyte subsets
218 are weak stimulators of naïve T-cells (22). Therefore, we finally opted to include only CD14⁺
219 monocytes as a reference monocyte population as these cells embody the ‘classical’ monocyte

220 subset (22). Single-cell transcriptome data confirmed that cDC1, cDC2, pDC and CD14⁺
221 monocytes each represent homogeneous cell populations. Furthermore, cells in the ‘activated
222 DC’ cluster expressed cDC2 and cDC1 hallmark genes, including *CD1c* and *IRF8* respectively
223 (Figure E1B). Therefore, this cluster represented a mixture of cDC1 and cDC2 with a distinct
224 activation status rather than a separate DC subset with a distinct ontogeny.

225 However, additional flow cytometry analysis revealed heterogeneous expression
226 of several myeloid cell markers by cDC2, including FcεRI, CD1a and the monocyte marker
227 CD14 (Figure E1C). This could imply potential presence of a CD14^{hi}FcεRI^{hi}CD1a^{hi} monocyte-
228 derived (mo)DC population within the cDC2 gate. However, CD14^{lo} and CD14^{hi} cDC2
229 fractions displayed a similar heterogeneous expression pattern of both FcεRI and CD1a, hence
230 we couldn’t identify a clear CD14^{hi}FcεRI^{hi}CD1a^{hi} subset (Figure E1D). Moreover, CD14^{lo} and
231 CD14^{hi} fractions exhibited a similar (cDC2) expression profile of the lineage-defining
232 transcription factors IRF4 and IRF8 (14), clearly distinct from that exhibited by CD14⁺
233 monocytes, considered as the precursors of moDC (14) (Figure E1D). Thus, there were no
234 immediate indications that the CD14⁺ cDC2 represent an ontogenetically different subset.
235 Moreover, full comprehension of the ontogenetic relationship between CD14^{lo} and CD14^{hi}
236 cDC2 fractions requires further investigation and is beyond the scope of this study. Therefore,
237 we decided to isolate the different lung DC subsets as outlined in Figure E1A.

238

239 **Lung cDC2 are the most potent subset to polarize naïve CD4⁺ T-cells into Tfh-like cells**

240 To assess the capacity of the different human lung DC subsets to polarize naïve
241 CD4⁺ T-cells into Tfh- or Tfh-like cells, FACS-sorted lung DC subsets were co-cultured with
242 allogeneic naïve blood CD4⁺ T-cell (MLR). The degree of Tfh-polarization was assessed at d7
243 of the culture. Compared to other DC subsets, cDC2 induced the highest proportion of CD4⁺
244 T-cells expressing high levels of ICOS and PD-1, two hallmark Tfh-markers (Figure 2A and

245 E2A). Of note, lung pDCs and CD14⁺ monocytes are poor stimulators of naïve CD4⁺ T-cell
246 proliferation (Figure E3A), underlying the lower proportions of ICOS^{hi}PD-1^{hi} T-cells in these
247 co-cultures. However, cDC2 and cDC1 induced similar levels of T-cell proliferation (Figure
248 E3A) implying that there was an intrinsic qualitative difference between both cDC subsets to
249 promote Tfh-like cell skewing. Compared to ICOS⁻PD-1⁺, ICOS⁺PD-1⁻ and ICOS⁻PD-1⁻ T-cell
250 subsets in the co-culture, ICOS^{hi}PD-1^{hi} T-cells were characterized by the highest surface levels
251 of OX40, another critical Tfh-cell marker (Figure 2B). Moreover, compared to the three other
252 T-cell populations, ICOS^{hi}PD-1^{hi} T-cells were the dominant producers of IL-21 and CXCL13,
253 the hallmark Tfh cytokine and chemokine respectively, confirming the Tfh-like cell nature of
254 this T-cell population (Figure 2C and E2B). In contrast, there was no significant difference in
255 secretion of the Th1 cytokine IFN- γ by ICOS^{hi}PD-1^{hi} T-cells as compared to ICOS⁻PD-1⁺ T-
256 cells (Figure E3B), demonstrating that the ICOS^{hi}PD-1^{hi} T-cells do not simply represent a
257 generally increased activation state. Importantly, compared to cDC1, lung cDC2 induced
258 increased proportions of ICOS^{hi}PD-1^{hi} IL-21 secreting T-cells (Figure 2D). Of note, there was
259 no significant difference in the induction of IFN- γ secretion by ICOS⁺PD-1⁺ T-cells induced by
260 cDC1 and cDC2, implying a degree of selectivity in the T-cell cytokine responses elicited by
261 cDC2 versus cDC1 (Figure E3C).

262 To further confirm the induction of Tfh-cells in the co-cultures, we analyzed
263 expression of CXCR5, a classical Tfh-cell surface marker, and Bcl6, key transcription factor
264 driving Tfh-cell development (23). Expression of CXCR5 was transient and not detectable at
265 day 7 (*data not shown* and (24)). Therefore, we determined the proportion of
266 CXCR5^{hi}ICOS^{hi}PD-1^{hi}Bcl6^{hi} Tfh-like cells in the different co-cultures at day 4, a time point
267 that corresponds with peak CXCR5 expression (24). In line with our previous results from day
268 7, cDC2 were the most efficient inducers of ICOS^{hi}CXCR5^{hi} T-cells as compared to cDC1, pDC
269 and CD14⁺ monocytes (Figure 2E and E2C). Importantly, in contrast to ICOS⁺CXCR5⁻ and

270 ICOS⁻CXCR5⁻, ICOS^{hi}CXCR5^{hi} T-cells were almost exclusively PD-1^{hi}Bcl6^{hi}, further
271 supporting their Tfh-like nature (Figure 2F and E2D).

272 Collectively, these results demonstrate that human resident lung cDC2 are the
273 most potent DC subset to polarize Tfh-like cells from naïve CD4⁺ T-cells.

274

275 **cDC2 from GOLD II COPD lungs show increased potential to induce Tfh-like cells,**
276 **which correlated with increased presence of Tfh-like cells in the lung tissue**

277 We next assessed whether lung cDC2 from COPD patients exhibited an increased
278 capacity to induce Tfh-like cells as compared to cDC2 from non-obstructed lungs. To this end,
279 we isolated cDC2 from GOLD II COPD peripheral lung tissue and co-cultured these cells with
280 allogeneic naïve blood CD4⁺ T-cells. COPD lung cDC2 induced increased proportions of Tfh-
281 like cells as compared to control cDC2 from non-obstructed lungs (Figure 3A and E4A).
282 Importantly, Tfh-like cells induced by COPD cDC2 contained an increase in the frequency of
283 IL-21⁺ cells as compared to Tfh-like cells induced by cDC2 from non-obstructed lungs (Figure
284 3B and E4B). Of note, the difference in Tfh-like cell induction between COPD and control
285 cDC2 could not be attributed to a difference in their potential to stimulate T-cell proliferation
286 (Figure E4C). Furthermore, control and COPD cDC2 contained a similar proportion of CD14^{hi}
287 cells, indicating that a difference in CD14^{hi} cDC2 fraction did not underlie the difference in
288 Tfh-like cell induction by control and COPD cDC2 (Figure E4D).

289 We next investigated whether there is a corresponding increased presence of Tfh-
290 like cells in peripheral lung tissue of GOLD II COPD subjects. Flow cytometry analysis
291 revealed the presence of ICOS^{hi}PD-1^{hi} T-cells in both control and COPD lung tissue.
292 Importantly, compared to control lungs, the frequency of ICOS^{hi}PD-1^{hi} T-cells was increased
293 GOLD II COPD lungs (Figure 3C and E4D). In line with our *in vitro* findings, lung ICOS^{hi}PD-
294 1^{hi} T-cells were the dominant IL-21 producers as compared to ICOS⁻PD-1^{hi}, ICOS^{hi}PD-1⁻ and
295 ICOS⁻PD-1⁻ T-cell fractions, confirming the Tfh-like nature of these cells (Figure 3D).

296

297 **Lung cDC2 express a unique migratory signature distinct from cDC1**

298 The chemoattractants CXCL12 and CXCL13 are instrumental for TLO-formation
299 during COPD by mediating the recruitment and localization of the critical cell types, including
300 T cells, B cells and DCs (7, 25, 26). Therefore, we analyzed expression of the corresponding
301 receptors CXCR4 and CXCR5 on cDC2 and cDC1 via flow cytometry. In control lungs, cDC2
302 tended to exhibit increased expression of CXCR5 while CXCR4 levels were significantly
303 increased as compared to cDC1 (Figure 4A and E5A). However, there was no difference in
304 CXCR5 and CXCR4 expression between control and COPD cDC2 (Figure E5B).

305 In addition, $7\alpha,25$ -dihydroxycholesterol, a cholesterol derivative, is a key
306 chemoattractant in organizing the lymphoid microenvironment (27). The receptor for $7\alpha,25$ -
307 dihydroxycholesterol, EBI2 (GPR183) is expressed on a variety of leukocytes, including T-
308 cells, B-cells, ILC3 and DC (27). Importantly, the oxysterol-EBI2 axis was recently shown to
309 be a key regulator of lung TLO formation in a mouse model of COPD (28). Moreover, EBI2
310 controls cDC2 positioning at the B-T zone border of mouse lymphoid organs (29). In non-
311 obstructed lungs, cDC2 expressed increased EBI2 surface levels as compared to cDC1 (Figure
312 4A). Of note, control and COPD cDC2 displayed similar expression levels of EBI2 (Figure
313 E5B). Additionally, we investigated the expression of EBI2 on T cell subsets in the peripheral
314 lung tissue in control and COPD subjects. Compared to $ICOS^-PD-1^{hi}$, $ICOS^{hi}PD-1^-$ and $ICOS^-$
315 $PD-1^-$ lung T-cells, the dominant IL-21 producing $ICOS^{hi}PD-1^{hi}$ T-cell fraction displayed the
316 highest levels of surface EBI2 as well (Figure 4B and E5C).

317 To further study the association between the oxysterole-EBI2 axis and TLO-
318 formation in COPD, we analyzed a publicly available dataset containing total lung
319 transcriptome data from a cohort of COPD patients (GOLD I – IV) and healthy control subjects
320 (Figure 4C) (GSE47460 derived from lung samples obtained through the NHLBI-funded Lung

321 Tissue Research Consortium (LTRC) as part of the Lung Genomic Research Consortium
322 (LGRC)). mRNA transcripts encoding *EBI2* and mRNA encoding enzymes in the cholesterol
323 metabolic pathway (i.e. *CH25H*, *CYP1B1* and *CYP7B1*) positively correlated with COPD
324 disease stage and hence inversely correlated with %FEV1 (Figure 4C). Importantly, lung *EBI2*,
325 *CH25H*, *CYP1B1* and *CYP7B1* mRNA expression all correlated with *CXCL13* mRNA
326 expression, a marker for TLO formation during COPD disease (Figure 4C). Finally, lung
327 *CH25H* mRNA strongly correlated with *EBI2* mRNA levels (Figure 4D).

328 The correlation between the oxysterole-EBI2 axis and TLO-formation
329 encouraged us to investigate the presence of the cholesterol metabolic pathway in TLOs of end-
330 stage (GOLD IV) COPD patients. Indeed, RNAscope analysis of lung TLOs confirmed the
331 expression of *CH25H* mRNA, encoding for one of the upstream enzyme involved in cholesterol
332 degradation (27) in both the B cell follicular area and the T cell zone of the TLO (Figure 4E).

333 Finally, we performed confocal imaging of GOLD IV COPD lung tissue to
334 determine the anatomical localization of cDC2 in the TLOs. This immunofluorescence analysis
335 showed that cDC2 were indeed abundantly present in the follicular T cell zone of the TLOs,
336 linking the unique migratory signature of cDC2 to the actual presence of these cells to TLOs
337 during COPD (Figure 5).

338

339 **Lung cDC2 express increased levels of OX40L and transcriptional signatures related to** 340 **Tfh-cell priming**

341 To gain insights into the mechanism used by cDC2 to induce Tfh-like cells, we
342 performed flow cytometric analysis of the co-stimulatory repertoire expressed on the different
343 lung DC subsets. ICOSL, PDL1 and OX40L are known to deliver critical co-stimulatory signals
344 to skew naïve T cells into Tfh-cells (23, 24). In non-obstructed control lungs, cDC2 and cDC1
345 subsets expressed similar levels of ICOSL and PDL1. However, we observed a significant

346 increase in OX40L expression in cDC2 cells as compared to cDC1 (Figure 6A). Importantly,
347 compared to control cDC2s, OX40L levels were even further increased on COPD cDC2 (Figure
348 6B). We next investigated whether OX40L was involved in Tfh-like cell polarization by lung
349 cDC2. cDC2 isolated from non-obstructed control lung tissue were co-cultured with allogeneic
350 naïve CD4⁺ T-cells in the presence of a blocking antibody for OX40L (oxelumab) or IgG
351 isotype control. ICOS⁺PD-1⁺ Tfh-like cell priming was analyzed at d7 of the co-culture.
352 Compared to the IgG control, blocking OX40L reduced ICOS⁺PD-1⁺ Tfh-like cell induction in
353 each experiment (Figure 6C), confirming the importance of the OX40L-OX40 axis.

354 To further understand the mechanisms underlying the enhanced ability of cDC2
355 to polarize Tfh-like cells, we compared the transcriptional profile of cDC2 with cDC1. cDC2
356 and cDC1 were FACS-sorted and their transcriptomic profile was generated via Next
357 Generation Sequencing (NGS). Interestingly, this analysis revealed that genes encoding for
358 signaling components of the IL-6 ($p = 0,0002$) and IL-1 ($p = 0,02$) pathways, critical for Tfh-
359 cell development (30, 31), were significantly upregulated in cDC2 (Figure 6D). Furthermore,
360 transcripts involved in general DC maturation and activation, features of DC contributing to
361 Tfh generation (32) were also upregulated in cDC2 compared to cDC1 (Figure 6D). Consistent
362 with these observations, biocomputational analysis identified signaling through CD40 ($p = 1,15$
363 $\times 10^{-10}$); secretion of multiple effector cytokines such as TNF ($p = 1,58 \times 10^{-22}$), IL-1 β ($p = 6,01$
364 $\times 10^{-21}$), IL-6 ($p = 2,86 \times 10^{-8}$) and IL-18 ($p = 9,43 \times 10^{-5}$) and transcription factors and signaling
365 mediators like NF- κ B ($p = 4,36 \times 10^{-14}$), STAT3 ($p = 4,06 \times 10^{-10}$) and ID3 ($p = 5,96 \times 10^{-5}$) as
366 putative upstream regulators of transcriptional signatures in lung cDC2 (Figure 6E). In contrast,
367 transcriptional pathways and genes downregulated in cDC2 had no immediate connection to
368 Tfh-priming by DC or were negatively associated with Tfh polarization, eg. LXR ($p = 9,54 \times$
369 10^{-5}) (33) (Figure 6E). Collectively, transcriptomic analysis indicates that lung cDC2 are

370 characterized by signatures related to key pathways involved in Tfh- or Tfh-like cell
371 polarization.

372 Discussion

373 The current study reveals a potent ability for cDC2 to induce IL-21 and CXCL13
374 secreting Tfh-like cells, suggesting a crucial role for cDC2 in TLO formation during COPD.

375 ScRNA-seq revealed a high level of heterogeneity among human lung Lin⁻HLA-
376 DR⁺ cells. In agreement with previous studies investigating human blood and lung tumor
377 myeloid cell heterogeneity (20, 21), we identified clusters of cDC1, cDC2, pDC, a cluster
378 containing ‘activated DC’, the three monocyte subsets, being CD14⁺ (‘classical’) monocytes,
379 CD16⁺ (‘non-classical’) monocytes and CD14⁺⁺CD16⁺ (‘intermediate’) monocytes and several
380 additional monocyte/macrophage populations. Furthermore, we found a population of NK-
381 cells, mast cells, type II AEC and endothelial cells. HLA-DR expression by NK-cells and mast
382 cells was reported previously (34, 35). Although type II AEC and endothelial cells can express
383 HLA-DR (36, 37) we believe that these rather represented a minor contamination. Compared
384 to the Zilionis *et al.* study, we found less monocyte/macrophage populations/phenotypes in the
385 lung tissue. This discrepancy could be explained by the fact that alveolar cells, containing
386 multiple alveolar macrophage phenotypes, were not part of our analysis. Furthermore, we
387 sampled lung tissue distant from the tumor bed, likely lacking several tumor-infiltrating
388 myeloid cell populations (TIMs) (21). Finally, this dataset has some limitations that warrant
389 future investigations, notably the lack of a larger validation cohort, the relatively low numbers
390 of cells analyzed and the read-depth which might have limited the power to define lung cell
391 subsets in this experiment.

392 The role of DC during COPD remains controversial. Several studies demonstrated
393 that DC exhibit an increased co-stimulatory repertoire (38) and that, especially CD1c⁺ DC
394 (cDC2), drive Th17-responses during cigarette smoke induced lung emphysema in both humans
395 and mice (39-42). In contrast, a recent report stated that human lung CD1c⁺ DC displayed a
396 regulatory function during COPD, suppressing pathogenic T-cell responses and inducing

397 regulatory T-cells (43). In our study, compared to other DC subsets, cDC2 were the most potent
398 in skewing naïve CD4⁺ T-cells into IL-21 and CXCL13 secreting Tfh-like cells. These findings
399 are in line with a recent murine study, demonstrating that lung cDC2, but not cDC1, were
400 driving antigen-specific Tfh-induction (44). Furthermore, recent research showed that human
401 tonsil cDC2 were the most efficient in Tfh-cell polarization as well (45). Strikingly, by using
402 lung resident cDC2 in our study, we also demonstrated that human cDC2 residing in non-
403 lymphoid peripheral organs can induce Tfh-like cells without requirement of prior migration to
404 draining lymph nodes.

405 The increased capability of COPD cDC2 to induce Tfh-like cells was associated
406 with increased presence of Tfh-like cells in the COPD parenchyma. To our knowledge, we are
407 the first to demonstrate the presence of a Tfh-like cell during early (GOLDI/II) stages of COPD.
408 We and others showed already the presence of peripheral, extrafollicular IL-21 secreting PD-
409 1⁺ICOS⁺ Tfh-like cells, that lack CXCR5 and/or Bcl6 expression, in rheumatoid arthritis (10),
410 skin fibrosis (9) and an HDM-driven asthma model (11). The effect of Tfh-like cells on COPD
411 development and progression remains to be elucidated. However, Ladjemi *et al* recently
412 confirmed the presence of IL-21⁺ T-cells that did not co-express CXCR5 in the TLOs of late-
413 stage COPD lungs, further supporting a role for an extrafollicular Tfh-like cell type and IL-21
414 (3).

415 cDC2 exhibited a unique migratory signature, including increased expression of
416 CXCR4, CXCR5 and EBI2, suggesting that these cells efficiently migrate to the site of TLO
417 formation during COPD. Levels of CXCL12 and CXCL13, ligands for CXCR4 and CXCR5
418 respectively, are increased in human COPD lungs (7, 25, 26). A recent study also highlighted
419 the crucial role of the oxysterol-EBI2 axis in COPD TLO formation (28). We now demonstrated
420 the presence of *CH25H* mRNA in both T- and B-cell zone of TLOs during late-stage COPD.
421 These results imply that cholesterol metabolism is important for maintaining the structure of

422 established TLO as well by continuously recruiting T-, B-cells and cDC2. In line with this
423 premise, we were able to detect cDC2 in the T-cell zone of GOLD IV COPD lung TLO. This
424 observation indicates that cDC2 are also important for maintaining established TLOs most
425 likely via sustained antigen-presentation and induction of T(fh-like) cell polarization and
426 proliferation.

427 Furthermore, we found that, compared to cDC1, cDC2 exhibited increased
428 (transcriptional) expression of pathways and genes related to DC-induced Tfh-priming,
429 including OX40L. In agreement with previous reports (24, 46), we confirmed that the OX40L-
430 OX40 axis promoted human Tfh-polarization. Mediators that stimulate OX40L expression,
431 including TSLP, IL-1, IL-33 and GM-CSF, are abundantly present in the lung (47, 48) and
432 elevated levels are observed in COPD subjects (47, 49, 50), likely underlying the increased
433 OX40L levels expressed by COPD cDC2. Additionally, several genes encoding for cytokine
434 mediators that deliver Tfh-skewing signals, including IL-6, IL-1 β and TGF β have already been
435 shown to be increased during COPD (51). This implies that these signals might further expand
436 the cDC2-induced Tfh-like cell polarization during COPD.

437 Collectively, we propose a model (Figure 7) in which, during COPD, locally
438 produced chemokines, like CXCL12 and CXCL13, and cholesterol metabolites attract cDC2
439 and CD4⁺ T-cells to the site of TLO formation. Upon encounter, cDC2 skew IL-21⁺ Tfh-like
440 cell polarization via OX40L and cytokine signals. Finally, the chronicity of this self-amplifying
441 loop results in the formation of well-organized TLOs in which Tfh-like cell clonality and
442 proliferation is further sustained by cDC2. Thus, our study reveals a new (immune) mechanism
443 underlying TLO formation during COPD. However, additional studies will be required to fully
444 comprehend the role of this pathway, and of TLO formation in general, in COPD pathogenesis
445 and progression.

446

447 **Acknowledgments**

448 We are grateful to all the lung tissue donors. We thank the surgeons and nurses from the
449 Thoraxkliniken, Sahlgrenska University Hospital and Gothenburg University, Gothenburg,
450 Sweden for sample collection. We also wish to thank Mr Aiman Alzetani, Professor Christian
451 Ottensmeier and the rest of the Target Lung team for sample collection in Southampton.

452 References

- 453
454 1. Collaborators GBDCoD. Global, regional, and national age-sex specific mortality for 264 causes of
455 death, 1980-2016: a systematic analysis for the Global Burden of Disease Study 2016. *Lancet*
456 2017; 390: 1151-1210.
- 457 2. Hogg JC, Chu F, Utokaparch S, Woods R, Elliott WM, Buzatu L, Cherniack RM, Rogers RM, Sciurba FC,
458 Coxson HO, Pare PD. The nature of small-airway obstruction in chronic obstructive pulmonary
459 disease. *N Engl J Med* 2004; 350: 2645-2653.
- 460 3. Ladjemi MZ, Martin C, Lecocq M, Detry B, Aboubakar Nana F, Moulin C, Weynand B, Fregimilicka C,
461 Bouzin C, Thurion P, Carlier F, Serre J, Gayan-Ramirez G, Delos M, Ocak S, Burgel PR, Pilette C.
462 Increased IgA Expression in Lung Lymphoid Follicles in Severe COPD. *Am J Respir Crit Care Med*
463 2018.
- 464 4. Polverino F, Cosio BG, Pons J, Laucho-Contreras M, Tejera P, Iglesias A, Rios A, Jahn A, Sauleda J, Divo
465 M, Pinto-Plata V, Sholl L, Rosas IO, Agusti A, Celli BR, Owen CA. B Cell-Activating Factor. An
466 Orchestrator of Lymphoid Follicles in Severe Chronic Obstructive Pulmonary Disease. *Am J*
467 *Respir Crit Care Med* 2015; 192: 695-705.
- 468 5. Randall TD. Bronchus-associated lymphoid tissue (BALT) structure and function. *Adv Immunol* 2010;
469 107: 187-241.
- 470 6. John-Schuster G, Hager K, Conlon TM, Irmeler M, Beckers J, Eickelberg O, Yildirim AO. Cigarette
471 smoke-induced iBALT mediates macrophage activation in a B cell-dependent manner in COPD.
472 *Am J Physiol Lung Cell Mol Physiol* 2014; 307: L692-706.
- 473 7. Bracke KR, Verhamme FM, Seys LJ, Bantsimba-Malanda C, Cunoosamy DM, Herbst R, Hammad H,
474 Lambrecht BN, Joos GF, Brusselle GG. Role of CXCL13 in cigarette smoke-induced lymphoid
475 follicle formation and chronic obstructive pulmonary disease. *Am J Respir Crit Care Med* 2013;
476 188: 343-355.
- 477 8. Seys LJ, Verhamme FM, Schinwald A, Hammad H, Cunoosamy DM, Bantsimba-Malanda C, Sabirsh A,
478 McCall E, Flavell L, Herbst R, Provoost S, Lambrecht BN, Joos GF, Brusselle GG, Bracke KR. Role
479 of B Cell-Activating Factor in Chronic Obstructive Pulmonary Disease. *Am J Respir Crit Care Med*
480 2015; 192: 706-718.
- 481 9. Taylor DK, Mittereder N, Kuta E, Delaney T, Burwell T, Dacosta K, Zhao W, Cheng LI, Brown C, Boutrin
482 A, Guo X, White WI, Zhu J, Dong H, Bowen MA, Lin J, Gao C, Yu L, Ramaswamy M, Gaudreau
483 MC, Woods R, Herbst R, Carlesso G. T follicular helper-like cells contribute to skin fibrosis. *Sci*
484 *Transl Med* 2018; 10.
- 485 10. Rao DA, Gurish MF, Marshall JL, Slowikowski K, Fonseka CY, Liu Y, Donlin LT, Henderson LA, Wei K,
486 Mizoguchi F, Teslovich NC, Weinblatt ME, Massarotti EM, Coblyn JS, Helfgott SM, Lee YC, Todd
487 DJ, Bykerk VP, Goodman SM, Pernis AB, Ivashkiv LB, Karlson EW, Nigrovic PA, Filer A, Buckley
488 CD, Lederer JA, Raychaudhuri S, Brenner MB. Pathologically expanded peripheral T helper cell
489 subset drives B cells in rheumatoid arthritis. *Nature* 2017; 542: 110-114.
- 490 11. Coquet JM, Schuijs MJ, Smyth MJ, Deswarte K, Beyaert R, Braun H, Boon L, Karlsson Hedestam GB,
491 Nutt SL, Hammad H, Lambrecht BN. Interleukin-21-Producing CD4(+) T Cells Promote Type 2
492 Immunity to House Dust Mites. *Immunity* 2015; 43: 318-330.
- 493 12. Perros F, Dorfmueller P, Montani D, Hammad H, Waelput W, Girerd B, Raymond N, Mercier O,
494 Mussot S, Cohen-Kaminsky S, Humbert M, Lambrecht BN. Pulmonary lymphoid neogenesis in
495 idiopathic pulmonary arterial hypertension. *Am J Respir Crit Care Med* 2012; 185: 311-321.
- 496 13. Guilliams M, Ginhoux F, Jakubzick C, Naik SH, Onai N, Schraml BU, Segura E, Tussiwand R, Yona S.
497 Dendritic cells, monocytes and macrophages: a unified nomenclature based on ontogeny. *Nat*
498 *Rev Immunol* 2014; 14: 571-578.
- 499 14. Guilliams M, Dutertre CA, Scott CL, McGovern N, Sichien D, Chakarov S, Van Gassen S, Chen J,
500 Poidinger M, De Prijck S, Tavernier SJ, Low I, Irac SE, Mattar CN, Sumatoh HR, Low GHL, Chung
501 TJK, Chan DKH, Tan KK, Hon TLK, Fossum E, Bogen B, Choolani M, Chan JKY, Larbi A, Luche H,
502 Henri S, Saeyes Y, Newell EW, Lambrecht BN, Malissen B, Ginhoux F. Unsupervised High-

- 503 Dimensional Analysis Aligns Dendritic Cells across Tissues and Species. *Immunity* 2016; 45: 669-
504 684.
- 505 15. GeurtsvanKessel CH, Willart MA, Bergen IM, van Rijt LS, Muskens F, Elewaut D, Osterhaus AD,
506 Hendriks R, Rimmelzwaan GF, Lambrecht BN. Dendritic cells are crucial for maintenance of
507 tertiary lymphoid structures in the lung of influenza virus-infected mice. *J Exp Med* 2009; 206:
508 2339-2349.
- 509 16. Muniz LR, Pacer ME, Lira SA, Furtado GC. A critical role for dendritic cells in the formation of
510 lymphatic vessels within tertiary lymphoid structures. *J Immunol* 2011; 187: 828-834.
- 511 17. Halle S, Dujardin HC, Bakocevic N, Fleige H, Danzer H, Willenzon S, Suezer Y, Hammerling G, Garbi
512 N, Sutter G, Worbs T, Forster R. Induced bronchus-associated lymphoid tissue serves as a
513 general priming site for T cells and is maintained by dendritic cells. *J Exp Med* 2009; 206: 2593-
514 2601.
- 515 18. van Rijt LS, Vos N, Willart M, Muskens F, Tak PP, van der Horst C, Hoogsteden HC, Lambrecht BN.
516 Persistent activation of dendritic cells after resolution of allergic airway inflammation breaks
517 tolerance to inhaled allergens in mice. *Am J Respir Crit Care Med* 2011; 184: 303-311.
- 518 19. Naessens T MY, Hamrud E, Gehrman U, Mattsson J, Skogberg G, Israelsson E, Thörn K, Melville F,
519 Deys L, Bracke K, Staples K, Cunoosamy D, Brusselle G, Lambrecht B. Human lung CD1c
520 dendritic cells orchestrate lymphoid neogenesis during COPD. *ERJ* 2019.
- 521 20. Villani AC, Satija R, Reynolds G, Sarkizova S, Shekhar K, Fletcher J, Griesbeck M, Butler A, Zheng S,
522 Lazo S, Jardine L, Dixon D, Stephenson E, Nilsson E, Grundberg I, McDonald D, Filby A, Li W, De
523 Jager PL, Rozenblatt-Rosen O, Lane AA, Haniffa M, Regev A, Hacohen N. Single-cell RNA-seq
524 reveals new types of human blood dendritic cells, monocytes, and progenitors. *Science* 2017;
525 356.
- 526 21. Zilionis R, Engblom C, Pfirschke C, Savova V, Zemmour D, Saatcioglu HD, Krishnan I, Maroni G,
527 Meyerovitz CV, Kerwin CM, Choi S, Richards WG, De Rienzo A, Tenen DG, Bueno R, Levantini
528 E, Pittet MJ, Klein AM. Single-Cell Transcriptomics of Human and Mouse Lung Cancers Reveals
529 Conserved Myeloid Populations across Individuals and Species. *Immunity* 2019; 50: 1317-1334
530 e1310.
- 531 22. Boyette LB, Macedo C, Hadi K, Elinoff BD, Walters JT, Ramaswami B, Chalasani G, Taboas JM, Lakkis
532 FG, Metes DM. Phenotype, function, and differentiation potential of human monocyte
533 subsets. *PLoS One* 2017; 12: e0176460.
- 534 23. Crotty S. T follicular helper cell differentiation, function, and roles in disease. *Immunity* 2014; 41:
535 529-542.
- 536 24. Pattarini L, Trichot C, Bogiatzi S, Grandclaude M, Meller S, Keuylian Z, Durand M, Volpe E,
537 Madonna S, Cavani A, Chiricozzi A, Romanelli M, Hori T, Hovnanian A, Homey B, Soumelis V.
538 TSLP-activated dendritic cells induce human T follicular helper cell differentiation through
539 OX40-ligand. *J Exp Med* 2017; 214: 1529-1546.
- 540 25. Litsiou E, Semitekoulou M, Galani IE, Morianos I, Tsoutsas A, Kara P, Rontogianni D, Bellenis I,
541 Konstantinou M, Potaris K, Andreacos E, Sideras P, Zakyntinos S, Tsoumakidou M. CXCL13
542 production in B cells via Toll-like receptor/lymphotoxin receptor signaling is involved in
543 lymphoid neogenesis in chronic obstructive pulmonary disease. *Am J Respir Crit Care Med*
544 2013; 187: 1194-1202.
- 545 26. Roos AB, Sanden C, Mori M, Bjermer L, Stampfli MR, Erjefalt JS. IL-17A Is Elevated in End-Stage
546 Chronic Obstructive Pulmonary Disease and Contributes to Cigarette Smoke-induced
547 Lymphoid Neogenesis. *Am J Respir Crit Care Med* 2015; 191: 1232-1241.
- 548 27. Cyster JG, Dang EV, Reboldi A, Yi T. 25-Hydroxycholesterols in innate and adaptive immunity. *Nat*
549 *Rev Immunol* 2014; 14: 731-743.
- 550 28. Jia J, Conlon TM, Sarker RS, Tasdemir D, Smirnova NF, Srivastava B, Verleden SE, Gunes G, Wu X,
551 Prehn C, Gao J, Heinzlmann K, Lintelmann J, Irmeler M, Pfeiffer S, Schloter M, Zimmermann R,
552 Hrabe de Angelis M, Beckers J, Adamski J, Bayram H, Eickelberg O, Yildirim AO. Cholesterol
553 metabolism promotes B-cell positioning during immune pathogenesis of chronic obstructive
554 pulmonary disease. *EMBO Mol Med* 2018; 10.

- 555 29. Lu E, Dang EV, McDonald JG, Cyster JG. Distinct oxysterol requirements for positioning naive and
556 activated dendritic cells in the spleen. *Sci Immunol* 2017; 2.
- 557 30. Nish SA, Schenten D, Wunderlich FT, Pope SD, Gao Y, Hoshi N, Yu S, Yan X, Lee HK, Pasman L,
558 Brodsky I, Yordy B, Zhao H, Bruning J, Medzhitov R. T cell-intrinsic role of IL-6 signaling in
559 primary and memory responses. *Elife* 2014; 3: e01949.
- 560 31. Chakarov S, Fazilleau N. Monocyte-derived dendritic cells promote T follicular helper cell
561 differentiation. *EMBO Mol Med* 2014; 6: 590-603.
- 562 32. Yamasaki S, Shimizu K, Kometani K, Sakurai M, Kawamura M, Fujii SI. In vivo dendritic cell targeting
563 cellular vaccine induces CD4(+) Tfh cell-dependent antibody against influenza virus. *Sci Rep*
564 2016; 6: 35173.
- 565 33. Ryu H, Chung Y. Dyslipidemia promotes germinal center reactions via IL-27. *BMB Rep* 2018; 51:
566 371-372.
- 567 34. Erokhina SA, Streltsova MA, Kanevskiy LM, Telford WG, Sapozhnikov AM, Kovalenko EI. HLA-DR(+)
568 NK cells are mostly characterized by less mature phenotype and high functional activity.
569 *Immunol Cell Biol* 2018; 96: 212-228.
- 570 35. Lotfi-Emran S, Ward BR, Le QT, Pozez AL, Manjili MH, Woodfolk JA, Schwartz LB. Human mast cells
571 present antigen to autologous CD4(+) T cells. *J Allergy Clin Immunol* 2018; 141: 311-321 e310.
- 572 36. Taffin C, Favier B, Baudhuin J, Savenay A, Hemon P, Bensussan A, Charron D, Glotz D, Mooney N.
573 Human endothelial cells generate Th17 and regulatory T cells under inflammatory conditions.
574 *Proc Natl Acad Sci U S A* 2011; 108: 2891-2896.
- 575 37. Zissel G, Ernst M, Rabe K, Papadopoulos T, Magnussen H, Schlaak M, Muller-Quernheim J. Human
576 alveolar epithelial cells type II are capable of regulating T-cell activity. *J Investig Med* 2000; 48:
577 66-75.
- 578 38. Freeman CM, Martinez FJ, Han MK, Ames TM, Chensue SW, Todt JC, Arenberg DA, Meldrum CA,
579 Getty C, McCloskey L, Curtis JL. Lung dendritic cell expression of maturation molecules
580 increases with worsening chronic obstructive pulmonary disease. *Am J Respir Crit Care Med*
581 2009; 180: 1179-1188.
- 582 39. Shan M, Cheng HF, Song LZ, Roberts L, Green L, Hacken-Bitar J, Huh J, Bakaeen F, Coxson HO,
583 Storness-Bliss C, Ramchandani M, Lee SH, Corry DB, Kheradmand F. Lung myeloid dendritic
584 cells coordinately induce TH1 and TH17 responses in human emphysema. *Sci Transl Med* 2009;
585 1: 4ra10.
- 586 40. Shan M, You R, Yuan X, Frazier MV, Porter P, Seryshev A, Hong JS, Song LZ, Zhang Y, Hilsenbeck S,
587 Whitehead L, Zarinkamar N, Perusich S, Corry DB, Kheradmand F. Agonistic induction of
588 PPARgamma reverses cigarette smoke-induced emphysema. *J Clin Invest* 2014; 124: 1371-
589 1381.
- 590 41. Lu W, You R, Yuan X, Yang T, Samuel EL, Marcano DC, Sikkema WK, Tour JM, Rodriguez A,
591 Kheradmand F, Corry DB. The microRNA miR-22 inhibits the histone deacetylase HDAC4 to
592 promote T(H)17 cell-dependent emphysema. *Nat Immunol* 2015; 16: 1185-1194.
- 593 42. You R, Lu W, Shan M, Berlin JM, Samuel EL, Marcano DC, Sun Z, Sikkema WK, Yuan X, Song L, Hendrix
594 AY, Tour JM, Corry DB, Kheradmand F. Nanoparticulate carbon black in cigarette smoke
595 induces DNA cleavage and Th17-mediated emphysema. *Elife* 2015; 4: e09623.
- 596 43. Tsoumakidou M, Tousa S, Semitekolou M, Panagiotou P, Panagiotou A, Morianos I, Litsiou E,
597 Trochoutsou AI, Konstantinou M, Potaris K, Footitt J, Mallia P, Zakynthinos S, Johnston SL,
598 Xanthou G. Tolerogenic signaling by pulmonary CD1c+ dendritic cells induces regulatory T cells
599 in patients with chronic obstructive pulmonary disease by IL-27/IL-10/inducible costimulator
600 ligand. *J Allergy Clin Immunol* 2014; 134: 944-954 e948.
- 601 44. Krishnaswamy JK, Gowthaman U, Zhang B, Mattsson J, Szeponik L, Liu D, Wu R, White T, Calabro S,
602 Xu L, Collet MA, Yurieva M, Alsen S, Fogelstrand P, Walter A, Heath WR, Mueller SN, Yrlid U,
603 Williams A, Eisenbarth SC. Migratory CD11b(+) conventional dendritic cells induce T follicular
604 helper cell-dependent antibody responses. *Sci Immunol* 2017; 2.

- 605 45. Durand M, Walter T, Pirnay T, Naessens T, Gueguen P, Goudot C, Lameiras S, Chang Q, Talaei N,
606 Ornatsky O, Vassilevskaia T, Baulande S, Amigorena S, Segura E. Human lymphoid organ cDC2
607 and macrophages play complementary roles in T follicular helper responses. *J Exp Med* 2019.
- 608 46. Jacquemin C, Schmitt N, Contin-Bordes C, Liu Y, Narayanan P, Seneschal J, Maurouard T, Dougall D,
609 Davizon ES, Dumortier H, Douchet I, Raffray L, Richez C, Lazaro E, Duffau P, Truchetet ME,
610 Khoryati L, Mercie P, Couzi L, Merville P, Schaeveerbeke T, Viillard JF, Pellegrin JL, Moreau JF,
611 Muller S, Zurawski S, Coffman RL, Pascual V, Ueno H, Blanco P. OX40 Ligand Contributes to
612 Human Lupus Pathogenesis by Promoting T Follicular Helper Response. *Immunity* 2015; 42:
613 1159-1170.
- 614 47. Ying S, O'Connor B, Ratoff J, Meng Q, Fang C, Cousins D, Zhang G, Gu S, Gao Z, Shamji B, Edwards
615 MJ, Lee TH, Corrigan CJ. Expression and cellular provenance of thymic stromal lymphopoietin
616 and chemokines in patients with severe asthma and chronic obstructive pulmonary disease. *J*
617 *Immunol* 2008; 181: 2790-2798.
- 618 48. Naessens T, Schepens B, Smet M, Pollard C, Van Hoecke L, De Beuckelaer A, Willart M, Lambrecht
619 B, De Koker S, Saelens X, Grooten J. GM-CSF treatment prevents respiratory syncytial virus-
620 induced pulmonary exacerbation responses in postallergic mice by stimulating alveolar
621 macrophage maturation. *J Allergy Clin Immunol* 2016; 137: 700-709 e709.
- 622 49. Morissette MC, Shen P, Thayaparan D, Stampfli MR. Disruption of pulmonary lipid homeostasis
623 drives cigarette smoke-induced lung inflammation in mice. *Eur Respir J* 2015; 46: 1451-1460.
- 624 50. Kearley J, Silver JS, Sanden C, Liu Z, Berlin AA, White N, Mori M, Pham TH, Ward CK, Criner GJ,
625 Marchetti N, Mustelin T, Erjefalt JS, Kolbeck R, Humbles AA. Cigarette smoke silences innate
626 lymphoid cell function and facilitates an exacerbated type I interleukin-33-dependent
627 response to infection. *Immunity* 2015; 42: 566-579.
- 628 51. Barnes PJ. Inflammatory mechanisms in patients with chronic obstructive pulmonary disease. *J*
629 *Allergy Clin Immunol* 2016; 138: 16-27.

630

631 **Tables**

632

633 **Table 1: Summary of subject demographics, smoking history, and spirometry**

Group	Control	COPD GOLD II	COPD GOLD IV
Subjects, <i>n</i>	35	7	5
Sex: M,F	14, 21	3, 4	0, 5
Age, yr	65 (10)	70 (6)	61 (8)
Smoking, pack-years (active and former)	28 (12)	41 (10)	45 (9)
Smoking status: never, active, former	8, 1, 26	0, 0, 7	0, 0, 5
FEV ₁ , % pred	94 (17)	57 (7)	27 (17)
DL _{CO} , % pred	74 (14)	63 (10)	31 (4)

Definition of abbreviations: % pred = percentage of the predicted value; COPD = Chronic Obstructive Pulmonary Disease

Data are represented as mean (SD)

634

635 **Figure legends**

636

637 **Figure 1: Human non-obstructed lungs contain a highly heterogeneous myeloid cell**
638 **compartment.** Myeloid cells, purified from non-obstructed human peritumoral lung tissues
639 (n=3), were analyzed by single-cell RNA sequencing using the Seurat package. Combined
640 single-cell transcriptomes were analyzed. (A) t-SNE representation of cell clusters identified
641 using unsupervised clustering. Each dot represents an individual cell. Colors represent
642 identified clusters. (B) Heatmap of scaled expression of (log values of Unique Molecular
643 Identifiers (UMI)) for the top 20 differentially expressed genes of each cluster (based on log
644 fold change). (C) Signature scores (arbitrary units) of individual cells for indicated gene
645 signatures.

646

647 **Figure 2: Lung cDC2 are the most potent inducers of Tfh-like cell polarization.** DC subsets
648 were purified from non-obstructed peritumoral lung tissue and co-cultured with allogeneic
649 naïve blood CD4⁺ T-cells. (A) Percentages of ICOS⁺PD-1⁺ T-cells in the different DC/T-cell
650 co-cultures were determined at d7 of the co-culture via flow cytometry. Summary data graph
651 with each symbol representing an individual donor (n=10). (B) Flow cytometry histogram of
652 OX40 staining on ICOS⁺PD-1⁺ (purple), ICOS⁻PD-1⁺ (orange), ICOS⁺PD-1⁻ (blue) and ICOS⁻
653 PD-1⁻ (black) T-cell subsets in cDC2/T-cell co-cultures. Representative data from 3 donors is
654 shown. (C) Intracellular IL-21 (n=10) and CXCL13 (n=6) staining of ICOS⁺PD-1⁺ (purple),
655 ICOS⁻PD-1⁺ (orange), ICOS⁺PD-1⁻ (blue) and ICOS⁻PD-1⁻ (black) T-cell subsets in cDC2/T-
656 cell co-cultures after restimulation with PMA and ionomycin in the presence of Golgi-plug and
657 Golgi-stop. Summary data graph in which each symbol represents an individual donor. (D)
658 Percentages of ICOS⁺PD-1⁺IL-21⁺ T-cells in cDC2/T-cell and cDC1/T-cell co-cultures were
659 determined. Summary data graph in which each symbol represents an individual donor (n=10).

660 (E) Proportions of ICOS⁺CXCR5⁺ T-cells in the different DC/T-cell co-cultures were
661 determined at day 4. Summary data graph in which each symbol represents an individual donor
662 (n=6). (F) Percentages of PD-1^{hi}BCL6^{hi} cells in ICOS⁺CXCR5⁺, ICOS⁺CXCR5⁻ and ICOS⁻
663 CXCR5⁻ T-cell subsets in the cDC2/T-cell co-cultures were determined via flow cytometry.
664 Summary data graph in which each symbol represents an individual donor (n=6). *p<0.05,
665 **p<0.01, ***p<0.001, Tukey's multiple comparison test (A, C, E and F) and paired student's
666 *t*-test (D).

667

668 **Figure 3: cDC2 from COPD GOLD II lungs display increased potential to promote Tfh-**
669 **like cell skewing which is associated with the increased presence of Tfh-like cells in the**
670 **COPD lung.** (A) and (B) cDC2 were isolated from COPD GOLD II peritumoral lung tissues
671 (n=7) and co-cultured with allogeneic naïve CD4⁺ T-cells. Proportions of ICOS⁺PD-1⁺ T-cells
672 (A) and ICOS⁺PD-1⁺IL-21⁺ T-cells (B) were determined at day 7 and compared to the
673 respective T-cell proportions induced by cDC2 from non-obstructed peritumoral lung tissues
674 as previously shown in Figure 2 (n=10). Shown is summary data graphs in which each symbol
675 represents an individual donor. (C) Percentages of ICOS⁺PD-1⁺ Tfh-like cells were determined
676 in peritumoral lung tissue resections of COPD and non-obstructed control subjects via flow
677 cytometry. Shown is summary data graph in which each symbol represents an individual donor
678 (n=6 for controls and n=5 for COPD subjects). (D) Intracellular IL-21 staining of lung tissue
679 ICOS⁺PD-1⁺ (purple), ICOS⁻PD-1⁺ (orange), ICOS⁺PD-1⁻ (blue) and ICOS⁻PD-1⁻ (black) T-
680 cell subsets after PMA/ionomycin restimulation (+ Golgi-plug/Golgi-stop) in DC-free *in vitro*
681 cultures. Shown are pooled data from control (full diamonds) and COPD (open diamonds) lung
682 resections (n=11). Each symbol represents an individual donor. *p<0.05, **p<0.01,
683 ***p<0.001, Student's *t*-test (A-C) and Tukey's multiple comparison test (D).

684

685 **Figure 4: cDC2 exhibit a unique migratory pattern.** (A) Surface levels of CXCR5, CXCR4
686 and EBI2 were measured on cDC2 and cDC1 from non-obstructed peritumoral lung resections
687 via flow cytometry (n=7 for CXCR5, n=5 for CXCR4 and n=7 for EBI2). Summary data graphs
688 (mean MFI corrected for background intensity) for the indicated markers are shown. Each
689 symbol represents an individual donor. (B) Surface EBI2 levels on ICOS⁺PD-1⁺ (purple), ICOS⁻
690 PD-1⁺ (orange), ICOS⁺PD-1⁻ (blue) and ICOS⁻PD-1⁻ (black) T-cell subsets in the lung measured
691 via flow cytometry. Summary data graph (mean MFI corrected for background intensity) of
692 pooled control (full diamonds) and COPD (open diamonds) lung samples (n=10). Each symbol
693 represents an individual donor. (C) Correlations of whole lung *EBI2*, *CH25H*, *CYP1B1* and
694 *CYP7B1* mRNA expression with COPD disease severity (GOLD stage and %FEV1) and whole
695 lung *CXCL13* mRNA as a marker for TLO formation. (D) Correlation of whole lung *CH25H*
696 mRNA expression with whole lung *EBI2* mRNA expression. Data in C and D are derived from
697 a publicly available GSE-set (GSE47460). Healthy control subjects n=116; GOLD I n=24;
698 GOLD II n=97; GOLD III n=32 and GOLD IV n=54. (E) *In situ* visualization of *CH25H* mRNA
699 (brown) in COPD GOLD IV explanted lung tissue TLOs via RNAscope duplex technology
700 (n=5). *CD19* mRNA (red) is used to delineate the B-cell follicle of the TLO. *p<0.05, **p<0.01,
701 ***p<0.001, (A) Student's *t*-test, (B) Tukey's multiple comparison test (C) and Holm-Sidak's
702 multiple test correction was used. To test for correlation of expression for the indicated genes
703 within all study subjects, linear regression analysis and Pearson's correlation test were used to
704 calculate the correlation coefficient *r*, R² and p-value of correlation.

705

706 **Figure 5: cDC2 reside in the follicular T-cell zone of established COPD GOLD IV TLO.**
707 Representative confocal fluorescence images of TLOs located in COPD GOLD IV explanted
708 lungs (n=5). CD19 (blue) (AF594) and CD3ε (purple) (AF647) was used to define the B- and
709 T-cell zone of the TLO respectively. CD11c (green) (FITC) and CD1c (red) (AF542) were used

710 to identify cDC2 (white arrows). Hoechst was used as nuclear counter staining (grey). Scale
711 bars 100 μ m.

712

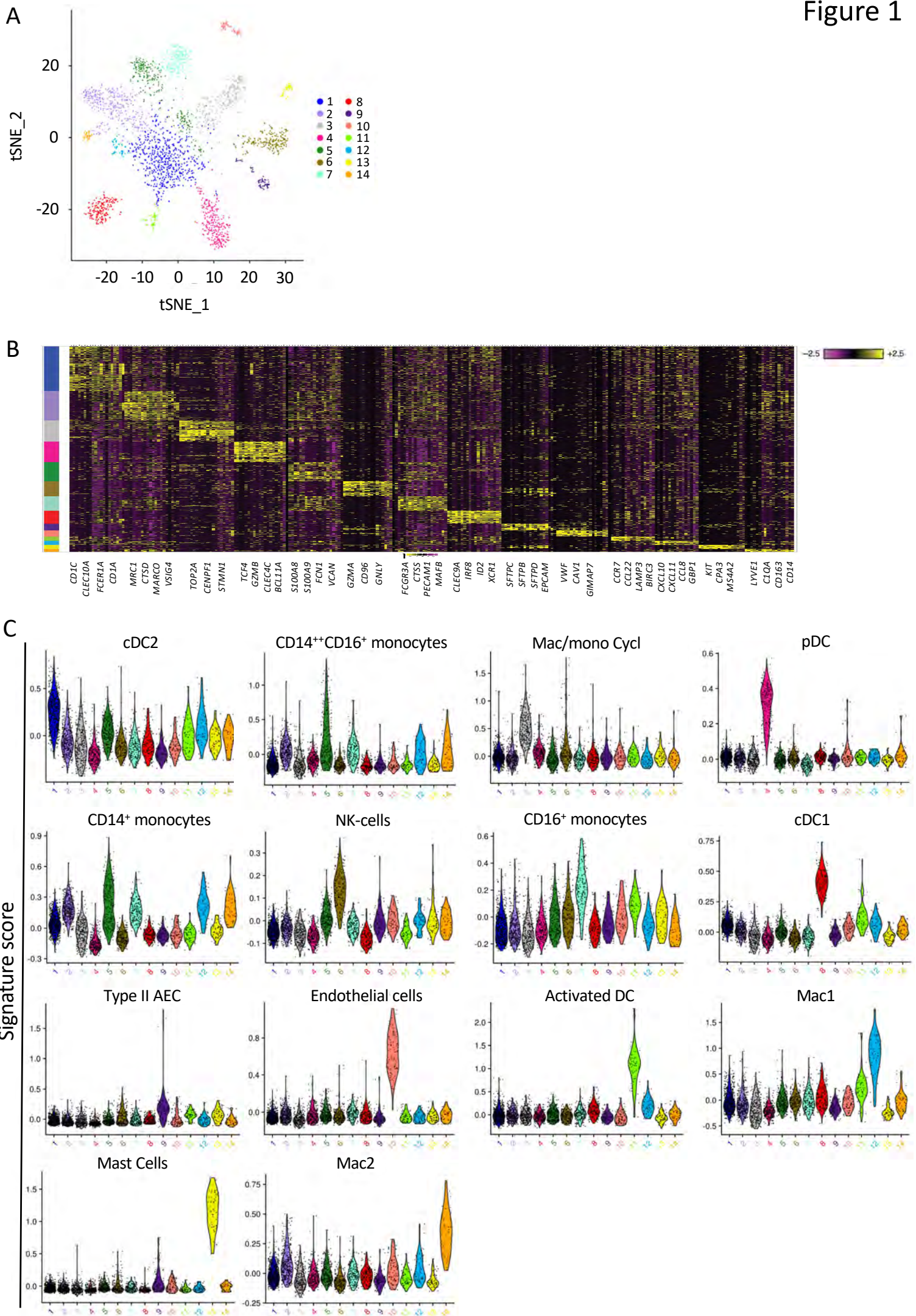
713 **Figure 6: cDC2 express increased levels of OX40L and transcriptional signatures related**
714 **to Tfh-cell priming.** Surface levels of ICOSL, PD-L1 and OX40L were measured on cDC2
715 and cDC1 from (A) non-obstructed and (B) COPD GOLDII (OX40L) peritumoral lung tissue
716 via flow cytometry. Summary data graphs of the indicated co-stimulatory markers are depicted
717 in A and representative flow cytometry histograms and summary data graph for OX40L is
718 shown in B. Each symbol represents an individual donor (n=5 for ICOSL, n=6 for PD-L1, n=7
719 for control OX40L control and n=5 for COPD OX40L). *p<0.05, **p<0.01, Student's *t*-test.
720 (C) cDC2 were isolated from non-obstructed peritumoral lung resections (n=3) and co-cultured
721 with allogeneic naïve CD4⁺ T-cells in the presence of an OX40L blocking antibody (oxelumab)
722 or an IgG isotype control. Proportions of ICOS⁺PD-1⁺ T-cells were determined at day 7. Shown
723 is the combined data graph in which each symbol represents an individual donor. (D) and (E)
724 cDC2 and cDC1 were FACS-sorted from non-obstructed peritumoral lung resections (n=5) and
725 the RNA transcriptomic profile of these subsets was generated via NGS. (D) Canonical
726 pathways significantly (signif) upregulated (red) and downregulated (blue) (Fisher's exact test,
727 $-\log_{10} P$ values for each represented pathway are shown) in transcriptional signatures in cDC2
728 vs cDC1 as predicted by Ingenuity Pathway Analysis (IPA). (E) Significant putative regulators
729 with predicted activating (red) or inhibitory (blue) influence on transcriptional signatures in
730 cDC2 vs cDC1 from non-obstructed lungs, as determined by IPA.

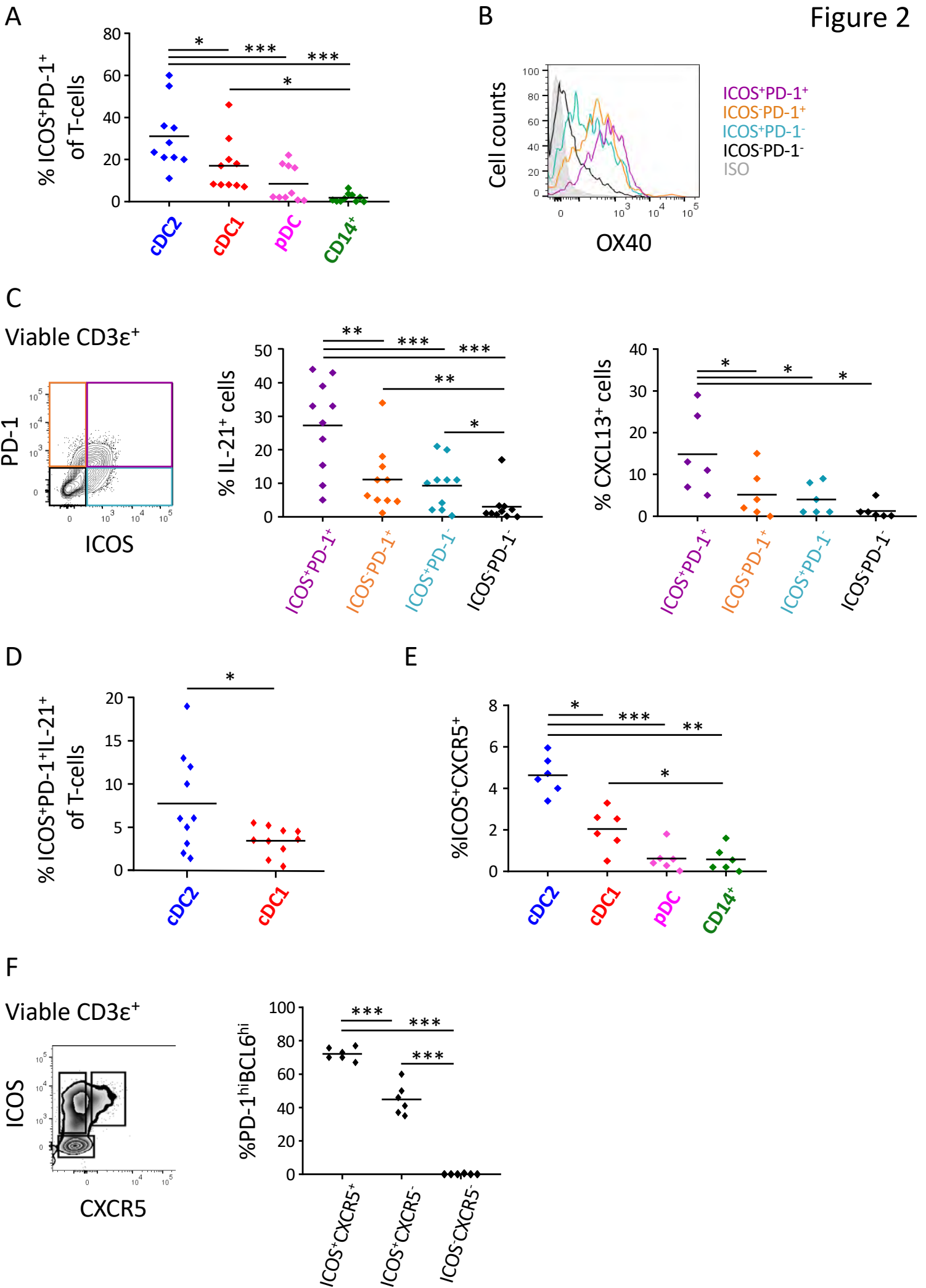
731

732 **Figure 7: cDC2 drive lymphoid neogenesis during COPD; a working model.** Elevated
733 pulmonary levels of CXCL12, CXCL13 and cholesterol metabolites, produced during COPD,
734 attract cDC2 and CD4⁺ T-cells to the site of TLO formation. Upon encounter, cDC2 drive IL-

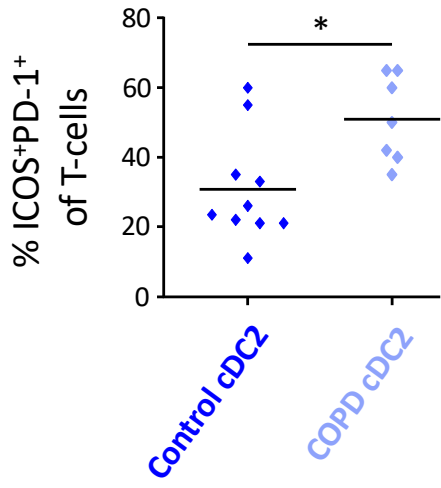
735 21⁺ Tfh-like cell polarization via the OX40L-OX40 axis and the secretion of cytokines like IL-
736 6, IL-1 β and TGF- β . The chronicity of this self-amplifying loop results in the formation of well-
737 established TLOs during late-stage COPD in which Tfh-like cell clonality and proliferation is
738 further sustained by cDC2.

Figure 1

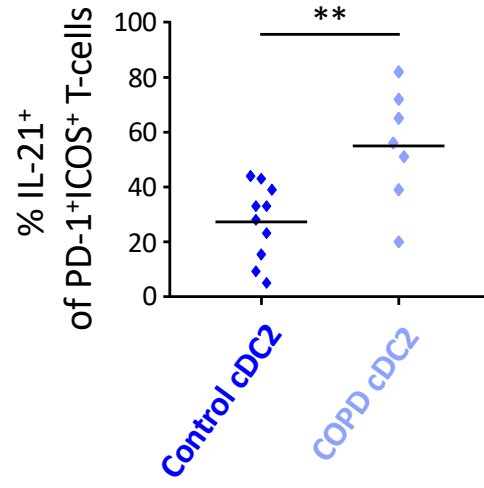




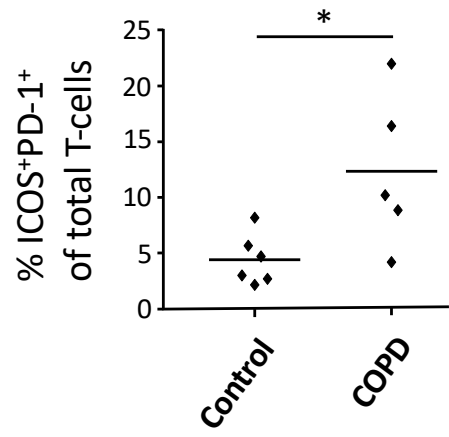
A



B



C



D

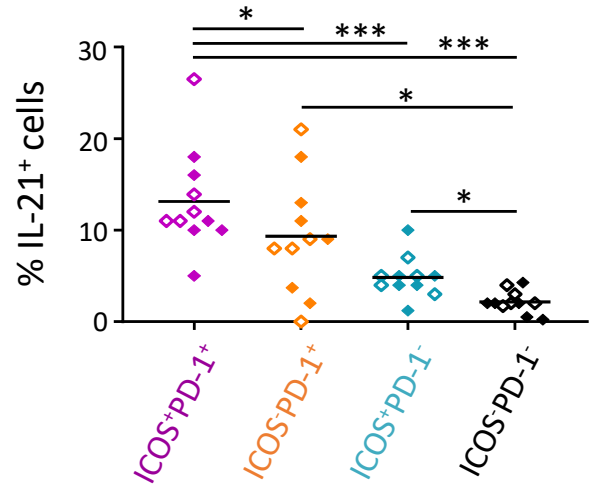
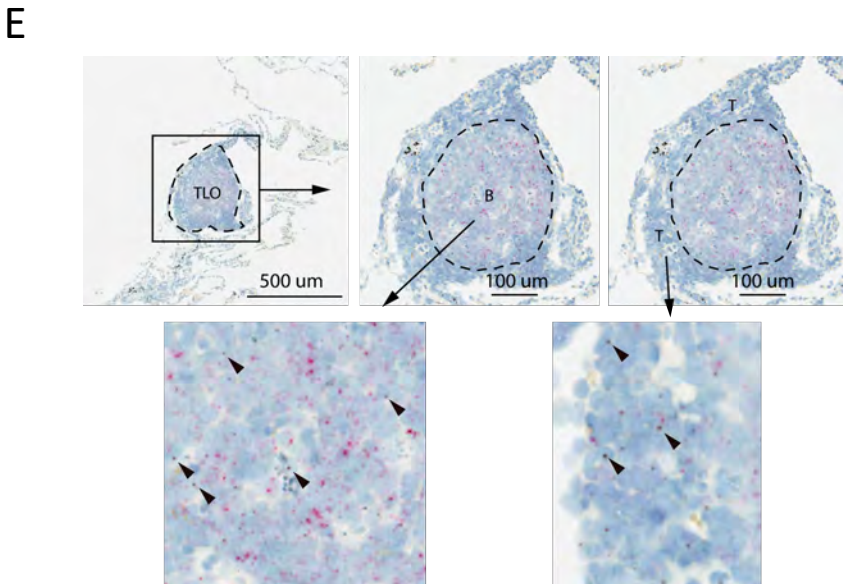
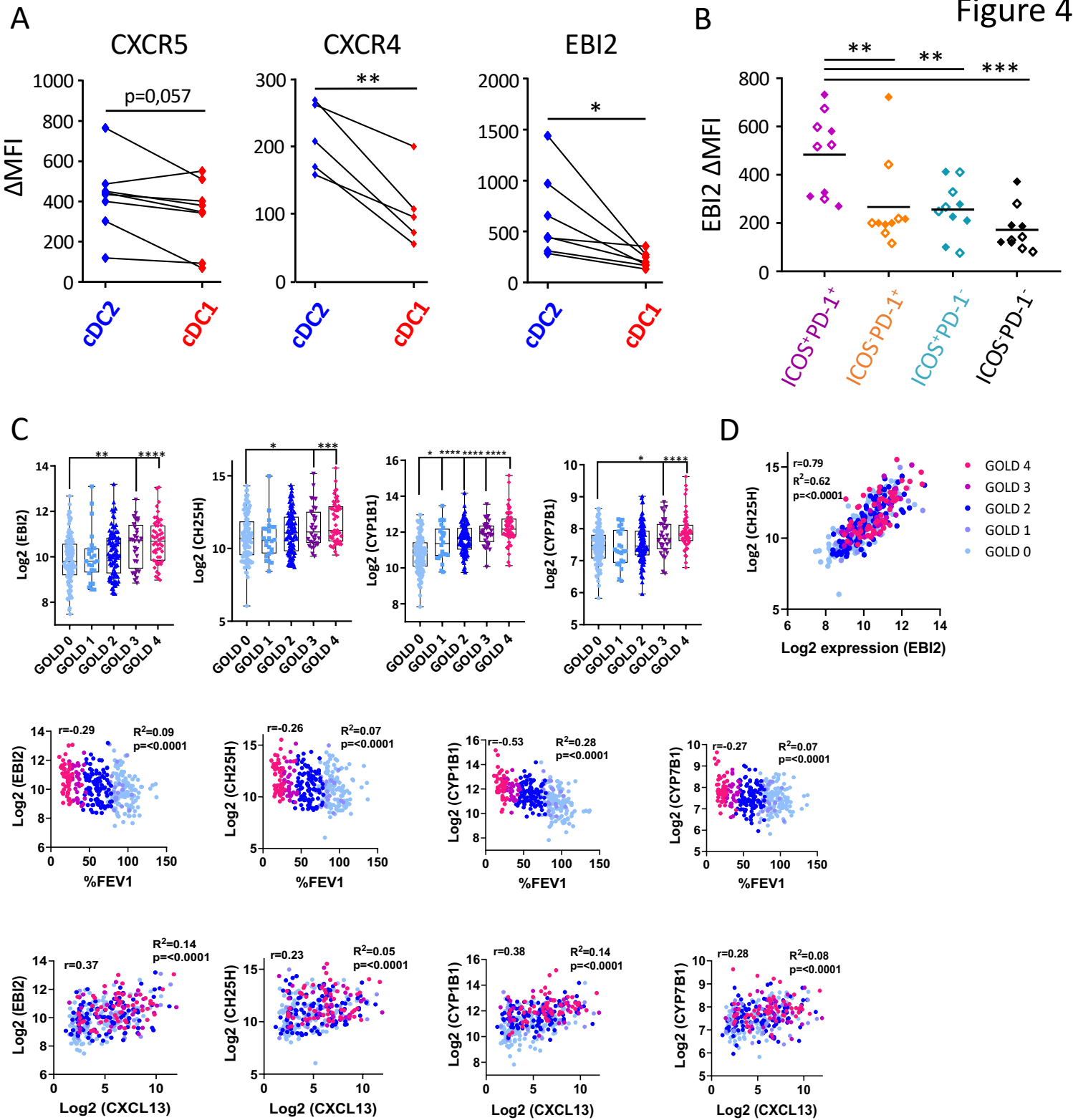
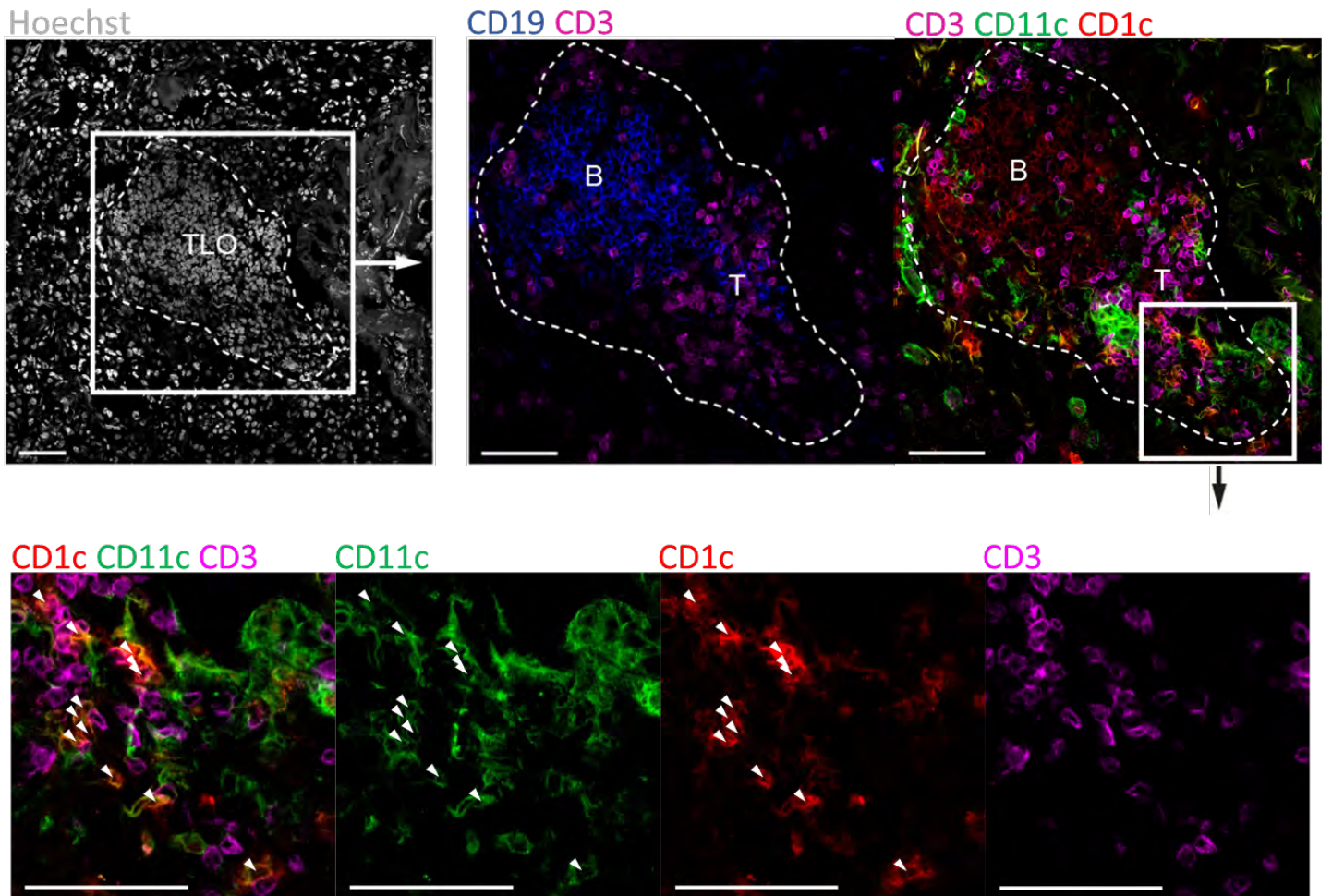


Figure 4





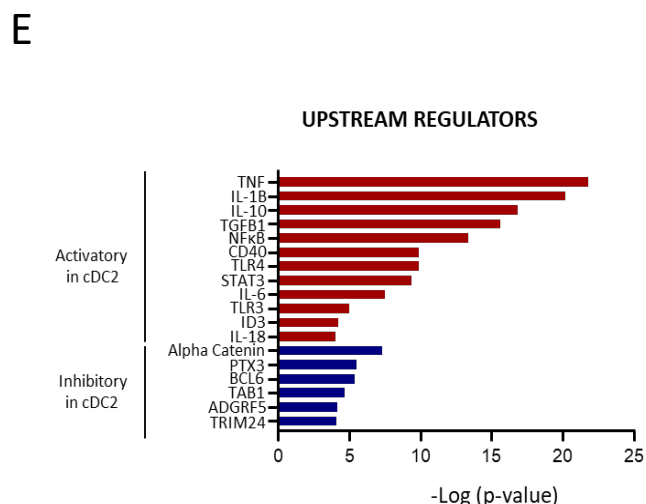
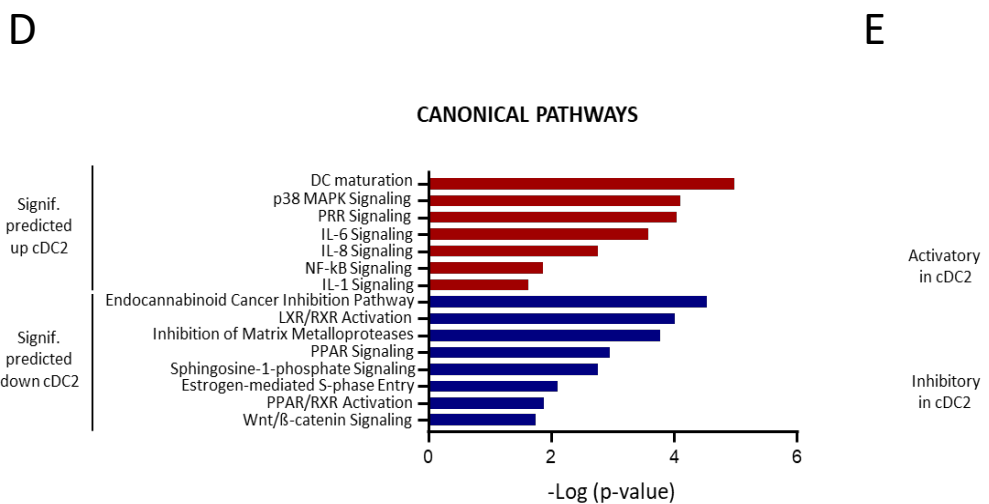
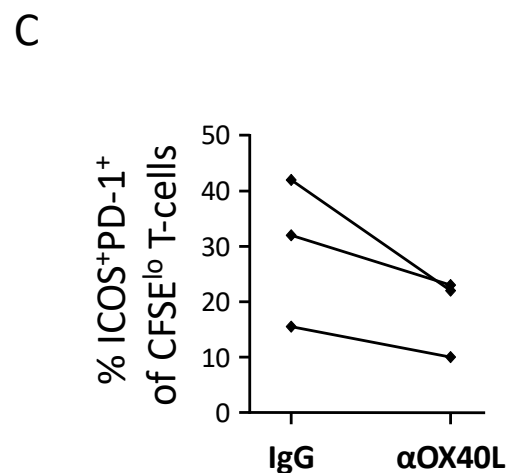
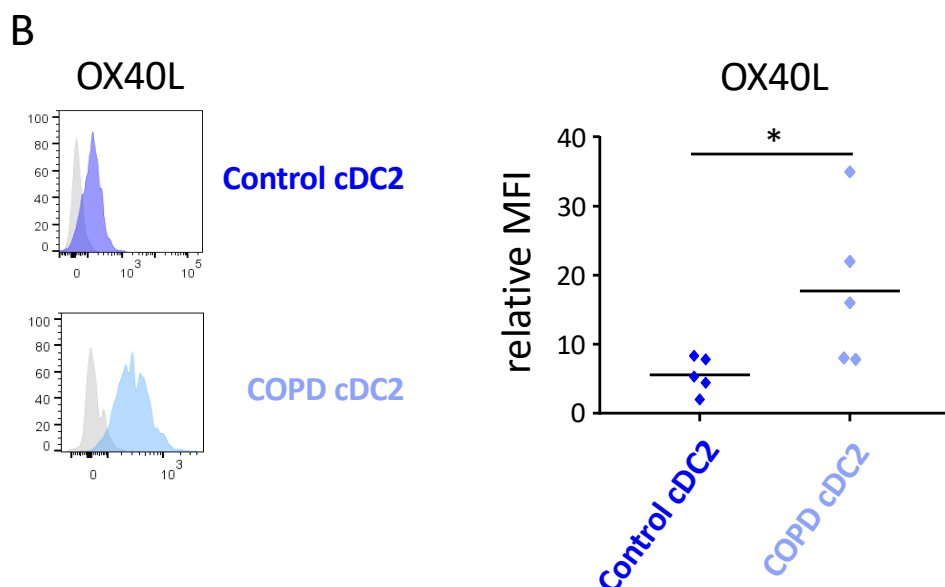
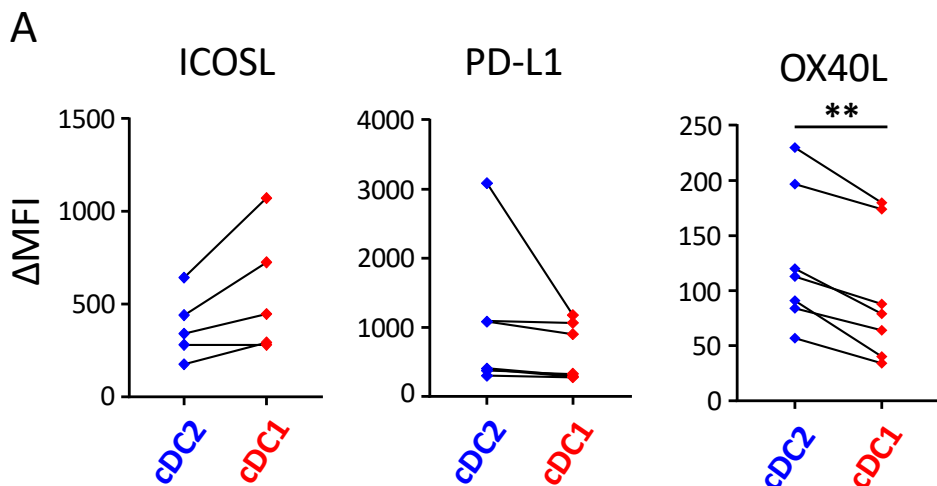
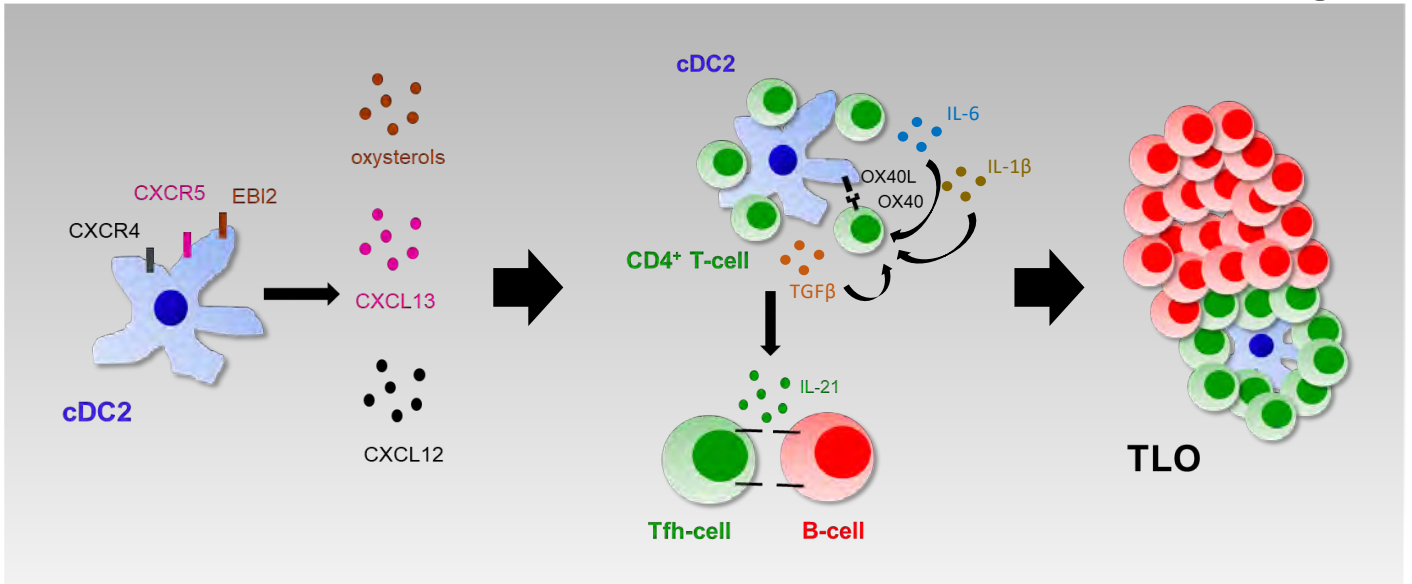


Figure 7



1 **Supplemental methods and results**

2

3 **Human lung conventional dendritic cells orchestrate lymphoid neogenesis during COPD**

4

5 **Authors:** Thomas Naessens, Yannick Morias*, Eva Hamrud*, Ulf Gehrman,
6 Ramachandramouli Budida, Johan Mattsson, Tina Baker, Gabriel Skogberg, Elisabeth
7 Israelsson, Kristofer Thörn, Martijn J. Schuijs, Bastian Angermann, Faye Melville, Karl J
8 Staples, Danen M Cunoosamy# and Bart N Lambrecht#

9

10 *Authors contributed equally to this paper

11 #Authors co-supervised the study

12 **Supplemental Methods**

13

14 **Human lung samples**

15 Lung samples were obtained from 35 non-obstructed control subjects (i.e. normal
16 lung function, among whom 8 never-smokers, 1 current smoker and 26 former smokers) and
17 12 patients with COPD undergoing lung surgery, either for resection of a solitary tumor (24
18 control subjects and 7 COPD GOLD II subjects) or transplantation for very severe COPD (5
19 COPD GOLD IV subjects) at the Sahlgrenska University Hospital, Gothenburg, Sweden. All
20 subjects underwent preoperative post-bronchodilator spirometry. Subjects were categorized by
21 based on the 2001 classification of the Global Initiative for Chronic Obstructive Lung Disease
22 (GOLD) (1). In case of resected tissue, macroscopically healthy lung was sampled. We defined
23 ex-smokers as having quit smoking habits for at least 6 months before surgery.

24

25 **Human lung sample processing**

26 Lung tissue was extensively flushed with PBS (Invitrogen) to remove excessive
27 blood contamination and alveolar cells. The flushed tissue was subsequently cut into small
28 pieces (0,5 cm x 0,5 cm) and incubated in a digestion buffer, containing 1mg/ml Collagenase
29 D (Sigma-Aldrich) in RPMI medium (Invitrogen), for 30 minutes at 37°C. Afterwards, the lung
30 tissue pieces were minced over a 100 µm cell strainer (Miltenyi Biotec) to obtain a single cell
31 suspension.

32

33 **Single-cell RNA sequencing of human lung myeloid cells**

34 FACS-sorted myeloid subpopulations were stained with Hoechst 33342 and
35 Propidium Iodide dye mix (Invitrogen, MA, USA) and diluted to 20,000 cells/mL. The cells
36 were dispensed into nanowells using the ICELL8 Single-Cell System (Takara Bio, Japan), and

37 single live cells were identified using CellSelect software (WaferGen, CA, USA). After a
38 freeze-thaw cycle, the cells were processed for RT-PCR and cDNA amplification according to
39 the manufacturer's instructions. The cDNA amplicons were then pooled and concentrated using
40 Zymo DNA Clean & ConcentratorTM-5 kit (Zymo Research, CA, USA) followed by cDNA
41 purification using 0.6X AMPure XP beads (Beckman Coulter, IN, USA) and quantification
42 using Qubit dsDNA HS Assay Kit on the Qubit fluorometer (Thermo Fisher, MA, USA). The
43 cDNA was quality checked using HS NGS kit on a Fragment Analyzer (Agilent, CA, USA).
44 The purified cDNA was subsequently used for Nextera XT (Illumina, CA, USA) library
45 preparation and amplification. A total of three lung tissues were processed individually for the
46 library preparation. The quality and quantity of the libraries was analyzed using HS NGS
47 Fragment Analyzer and Qubit dsDNA HS Assay Kit respectively. Sample libraries were pooled
48 in equimolar concentrations and diluted and denatured according to Illumina guidelines.
49 Sequencing was performed using a High Output 150 cycle kit on an Illumina NextSeq550 using
50 26 cycles for read1, and 126 cycles for read2.

51 ***Raw sequence processing and quality control.*** RNA-seq fastq files were
52 processed using bcbio-nextgen (version 1.1.0) (bcbio-nextgen. Validated, scalable, community
53 developed variant calling, RNA-seq and small RNA analysis. Available from:
54 <https://github.com/chapmanb/bcbio-nextgen>) where reads were mapped to the human genome
55 build hg38 (GRCh38.92 version 25) using hisat2 (version 2.1.0) (2). For the bulk dataset this
56 yielded between 37.2 – 64.9 M mapped reads per sample (with a mean of 49.4 M). No filtering
57 of samples or genes was performed on the bulk RNA sequencing data. For the single cell
58 dataset, 180 M reads aligned to genes. Gene level quantifications, counts and transcript per
59 million (TPM), were generated with featurecounts (version 1.4.4) (3) and sailfish (version
60 0.10.1) (4), respectively, all within bcbio. The single cell dataset was additionally
61 demultiplexed using UMIs with the umis (version 1.0.0), also within the bcbio framework.

62 Quality control included filtering by, the number of genes per cell, mitochondrial gene
63 contribution and minimum gene representation across cells.

64 ***Single cell sequencing data clustering and cluster identification.*** For the single
65 cell data, most analyses were performed using Seurat toolkit (4) (<https://satijalab.org/seurat/>,
66 version 3.1.0) available in R (R version 3.5.1). Single cell data was processed to regress out
67 unwanted sources of variation. Cells from the three donors were aggregated into separate Seurat
68 objects, these were then aligned to each other using canonical correlation analysis. Clustering
69 was conducted using a graph-based clustering approach within the framework of Seurat. 14
70 clusters that were found were used for all subsequent analysis and visualized using the Seurat
71 function *TSNEplot*. All plots were made using R (version 3.5.2, www.r-project.org) and Seurat
72 (version 3.1.0). Unique marker genes per cluster were extracted with the Seurat function
73 *FindAllMarkers* and the top 20 genes which displayed the highest log fold change in expression
74 between clusters were extracted. A phylogenetic tree relating to the ‘average’ cell from each
75 identity class was constructed from the dataset using the Seurat function *BuildClusterTree* and
76 the resulting scaled expression data for the top 20 genes per cluster were plotted using the Seurat
77 function *DoHeatmap*. To confirm cluster identities, published gene signatures for blood DC
78 subtypes from Villani *et al.* (5) and Zilionis *et al.* (6) were matched against our clusters. The
79 gene lists from Villani *et al.* were first filtered to remove any blood-specific genes that did not
80 appear in any of our single cell dataset. A signature score was then calculated for each signature
81 and cluster using the Seurat function *AddModuleScore*. Resulting scores were plotted using the
82 Seurat function *VlnPlot*.

83

84 **Next Generation RNA transcriptome Sequencing of human lung DC subsets**

85 ***Total RNA preparation.*** Sorted lung DC subsets were resuspended in 350 µl of
86 RLT Plus buffer (Qiagen) and stored at -80° C. Cell lysates were thawed, and total RNA was

87 extracted using RNeasy Plus Micro Kit (Qiagen) according to the manufacturer's protocol.
88 RNA quality and quantity were assessed on the Fragment Analyzer platform (AATI) using high
89 sensitivity RNA analysis kit. Only samples with RNA Integrity Number >8 were subsequently
90 used.

91 *Whole transcriptome profiling by RNA sequencing.* 1.5 ng of total RNA was used
92 as input to create total RNA libraries using Ovation® SoLo RNA-Seq System (NuGEN
93 Technologies) according to the manufacturer's protocol. Libraries were validated on the
94 Fragment Analyzer platform (AATI) using standard sensitivity NGS fragment analysis kit and
95 the concentration was determined using Quant-iT dsDNA High Sensitivity assay kit on the
96 Qubit fluorometer (Thermo Fisher). Sample libraries were pooled in equimolar concentrations,
97 diluted, and denatured according to Illumina guidelines. Sequencing was performed using a
98 High Output Kit v2 (150 cycles) on an Illumina NextSeq500.

99 *Data analysis.* The TPM (transcript per million) counts from the bulk RNA
100 sequencing dataset of the FACs-sorted cDC1, cDC2, pDC and CD14⁺ monocytes were log
101 transformed and expression of genes of interest were plotted as a heatmap using the function
102 *pheatmap* (7) (*pheatmap*: Pretty Heatmaps, version 0.12, [https://CRAN.R-](https://CRAN.R-project.org/package=pheatmap)
103 [project.org/package=pheatmap](https://CRAN.R-project.org/package=pheatmap)). Ingenuity Pathway Analysis (IPA; QIAGEN) was used to
104 functionally categorize differentially expressed genes and to biocomputationally identify
105 putative upstream regulators responsible for differential gene expression signatures.

106

107 **Flow cytometry**

108 *Extracellular surface marker staining.* Lung single cell suspensions were
109 incubated with Aqua LIVE/DEAD (Thermofisher) in PBS for 15 minutes at 4°C. After 2
110 washing steps with PBS, cells were stained in PBS containing 0,5% Fetal Calf Serum (FCS)
111 (Invitrogen) and 2mM EDTA (Invitrogen) with anti-human CD45-BV605 (clone HI30), HLA-

112 DR-BV786 (clone G46-6), CD3 ϵ -FITC (clone UCHT1), CD19-FITC (clone HIB19), CD56-
113 FITC (clone B159), CD66b-FITC (clone G10F5), CD16-PerCP-Cy5.5 (clone 3G8), CD11c-
114 PE-CF594 (clone B-ly6), CD141-BV711 (clone 1A4), CD3 ϵ -PE-CF594 (clone UCHT1),
115 ICOS-BV421 (clone DX29), CXCR5-PerCP-Cy5.5 (clone RF8B2), CXCR5-BUV395 (clone
116 RF8B2), CXCR4-BUV395 (clone 12G5), PD-L1-BUV395 (clone MIH1), Fc ϵ RI-PE (clone
117 AER37) (all from BD Biosciences), CD123-PE-Cy7 (clone 6H6), CD172a-APC (clone 15-
118 414), CD14-AF700 (clone 63D3), CD1c-BV421 (L161), CLEC9a-APC (clone 8F9), XCR1-
119 PE (clone S15046E), CD206-APC (clone 15-2), CD1a-PE-Cy7 (clone HI149), PD-1-BV711
120 (clone EH12.2H7), OX40-PE-Cy7 (clone Ber-ACT35), EBI2-PE (clone SA313E4), ICOSL-
121 PE-Cy7 (clone 2D3), CD1a-PE-Cy7 (clone HI149) (all from Biolegend) and OX40L-PE (clone
122 ANC10G1) (Ansell) for 30 minutes at 4°C.

123 *Intracellular cytokine staining.* To assess the expression of intracellular
124 cytokines, cells were stimulated with PMA (30ng/ml) and ionomycin (1 μ g/ml) (both from
125 Sigma) for 6h in the presence of GolgiPlug and GolgiStop (both from BD Biosciences) for the
126 last 4h. After stimulation, extracellular surface markers were stained before cells were fixed
127 and permeabilized (Fixation/Permeabilization Buffer Set, BD Biosciences). Next, cells were
128 stained with anti-human IL-21-eFluor660 (clone 3A3-N2) (eBioscience), CXCL13-PE (clone
129 53610) (R&D Systems) and IFN- γ -AF700 (clone B27) (BD Biosciences) for 30 minutes at 4°C
130 in Perm/Wash buffer (BD Biosciences).

131 *Intracellular transcription factor staining.* To assess the expression of
132 intracellular transcription factors, cells were stained for extracellular markers before fixation
133 and permeabilization (Fixation/Permeabilization Buffer Set, eBioscience). Next, cells were
134 stained with anti-human unconjugated Bcl6 (rabbit polyclonal) (Abcam), IRF4-PE-Cy7 (clone
135 3E4) and IRF8-APC (clone V3GYWCH) (both from eBioscience) for 30 minutes at 4°C in
136 Permeabilization Buffer (eBioscience). To detect the rabbit Bcl6, samples were incubated with

137 goat anti-rabbit IgG-PE (Invitrogen) for 15 minutes at 4°C in Permeabilization Buffer
138 (eBioscience).

139 All samples were acquired on a FACS Fortessa instrument (BD Biosciences) and
140 data was analyzed via FlowJo (Treestar).

141

142 **Lung DC subset FACS sorting**

143 The HLA-DR⁺ cell fraction was prepurified from total lung cells via the MACS
144 HLA-DR⁺ purification kit according to manufacturer's protocol (Miltenyi Biotec). HLA-DR⁺
145 cells were stained with Aqua LIVE/DEAD, anti-human CD45, HLA-DR, Lineage (CD3ε,
146 CD19, CD56, CD66b), CD11c, CD16, CD141, CD172a, CD1c, CD14 as previously described
147 in this online methods section. Subsequently, DC subsets were sorted with a FACS Aria III
148 instrument (BD Biosciences).

149

150 **Blood naïve CD4⁺ T cell isolation and CFSE labeling**

151 Peripheral blood was collected from healthy subjects via venous puncture in
152 Gothenburg, Sweden, under written informed consent. The study was reviewed and approved
153 by the ethical committee/review board in Gothenburg, Sweden, according to the Declaration of
154 Helsinki (number 033-10). Peripheral Blood Mononuclear Cells (PBMC) were prepared by
155 blood centrifugation on a Ficoll gradient (Lymphoprep, Greiner Bio-One). PBMCs were
156 viability frozen in Fetal Calf Serum (FCS) with 10% dimethyl sulfoxide (DMSO) (both
157 Invitrogen) until lung tissue was obtained from the Sahlgrenska Hospital (Gothenburg,
158 Sweden). Naïve CD4⁺ T cells were isolated from thawed PBMC aliquots by negative selection
159 using the Human Naïve CD4⁺ T Cell Isolation Kit according to the manufacturer's instructions
160 (Miltenyi Biotec). After isolation, cells were stained with 0,25µM CarboxyFluorescein
161 Succinimidyl Ester (CFSE) (eBioscience) for 10 minutes at room temperature in PBS

162 (Invitrogen). CD4⁺ T-cell purity and viability were assessed before each experiment via flow
163 cytometry.

164

165 **Mixed Leukocyte Reaction (MLR)**

166 Sorted lung DC (5000) were co-cultured with purified CFSE-labeled allogeneic
167 naïve blood CD4⁺ T-cells (25000) in RPMI medium supplemented with
168 Penicillin/Streptomycin, L-Glutamine and 10% heat-inactivated FCS (all from Invitrogen).
169 After 4 days or 6-7 days, intracellular Bcl6 expression and intracellular IL-21, CXCL13 and
170 IFN- γ levels respectively, were analyzed via flow cytometry as previously described in this
171 online methods section. In some experiments, 1 μ g/ml anti-human OX40L (oxelumab) or IgG
172 isotype control (both from Biovision) was added.

173

174 **RNAscope of GOLD IV COPD lung TLO**

175 Lung tissue biopsies were collected, fixed in formalin, dehydrated and embedded
176 in paraffin according to standard protocol. Blocks were cut into 4 μ m sections and placed on
177 superfrost plus glasses (ThermoFischer scientific). RNAscope 2.5 LS Duplex *in situ*
178 hybridization was performed according to manufacturer's protocol (Advanced Cell
179 Diagnostics, Newark, CA) on a Leica Bond Rx autostainer (Leica). Heat induced epitope
180 retrieval was performed for 15 minutes at 95°C using ER2 and protease was applied for 15
181 minutes. Probes used were: Hs-CD19 and Hs-CH25H. Chromogens applied were bond polymer
182 define detection (brown) and bond polymer refine red detection (both Leica Biosystems) and
183 sections were counterstained with hematoxylin. Slides were mounted using pertex mounting
184 medium and scanned on an aperio scan scope at 20x magnification.

185

186

187 **Fluorescence imaging of GOLD IV COPD lung TLO**

188 Lung tissue biopsies were collected and embedded in OCT. Blocks were cut into
189 4 µm sections and placed on superfrost plus glasses (ThermoFischer scientific). Samples were
190 fixed in acetone (Sigma-Aldrich) for 15 minutes at room temperature. Subsequently, samples
191 were blocked with IHC/ICC Blocking Buffer (eBioscience) for 15 minutes at room temperature.
192 Afterwards, samples were stained with CD3ε-AF647 (clone UCHT1), CD11c-FITC (clone B-
193 ly6) (both BD Biosciences), CD19-Biotin/AF594 (clone HIB19), CD1c-Biotin/AF542 (clone
194 L161) (both Biolegend) and Hoechst nuclear staining (Thermofisher Scientific). Biotin pre-
195 labeling with fluorochromes was performed using the Flexistain™ labeling kit according to the
196 manufacturer's protocol (Kromnigon AB, Sweden). Microscopy images were acquired using
197 an LSM 880 system (Carl Zeiss Microscopy, Germany) equipped with a Zeiss Image Z.1
198 microscope, Plan-Apochromat 40x/1,3 objective (Carl Zeiss Microscopy, Germany).
199 Brightness and contrast were adjusted using the Zen software (Black ed. v. 2,3, Carl Zeiss
200 Microscopy, Germany).

201

202 **Statistics**

203 Statistical analyses were calculated with GraphPad Prism (version 8) (GraphPad Software Inc,
204 US) and the tests used are mentioned in the figure legends. *P* values less than 0,05 were
205 considered as significant.

206 **References**

207

208 1. Pauwels RA, Buist AS, Calverley PM, Jenkins CR, Hurd SS, Committee GS. Global strategy for the
209 diagnosis, management, and prevention of chronic obstructive pulmonary disease.
210 NHLBI/WHO Global Initiative for Chronic Obstructive Lung Disease (GOLD) Workshop
211 summary. *Am J Respir Crit Care Med* 2001; 163: 1256-1276.

212 2. Kim D, Langmead B, Salzberg SL. HISAT: a fast spliced aligner with low memory requirements. *Nat*
213 *Methods* 2015; 12: 357-360.

214 3. Liao Y, Smyth GK, Shi W. featureCounts: an efficient general purpose program for assigning sequence
215 reads to genomic features. *Bioinformatics* 2014; 30: 923-930.

216 4. Patro R, Mount SM, Kingsford C. Sailfish enables alignment-free isoform quantification from RNA-
217 seq reads using lightweight algorithms. *Nat Biotechnol* 2014; 32: 462-464.

218 5. Villani AC, Satija R, Reynolds G, Sarkizova S, Shekhar K, Fletcher J, Griesbeck M, Butler A, Zheng S,
219 Lazo S, Jardine L, Dixon D, Stephenson E, Nilsson E, Grundberg I, McDonald D, Filby A, Li W, De
220 Jager PL, Rozenblatt-Rosen O, Lane AA, Haniffa M, Regev A, Hacohen N. Single-cell RNA-seq
221 reveals new types of human blood dendritic cells, monocytes, and progenitors. *Science* 2017;
222 356.

223 6. Zilionis R, Engblom C, Pfirschke C, Savova V, Zemmour D, Saatcioglu HD, Krishnan I, Maroni G,
224 Meyerovitz CV, Kerwin CM, Choi S, Richards WG, De Rienzo A, Tenen DG, Bueno R, Levantini
225 E, Pittet MJ, Klein AM. Single-Cell Transcriptomics of Human and Mouse Lung Cancers Reveals
226 Conserved Myeloid Populations across Individuals and Species. *Immunity* 2019; 50: 1317-1334
227 e1310.

228 7. Kolde R, Vilo J. GOsummaries: an R Package for Visual Functional Annotation of Experimental Data.
229 *F1000Res* 2015; 4: 574.

230

231 **Supplemental figure legends**

232

233 **Figure E1: Human non-obstructed lungs contain a highly heterogeneous myeloid cell**
234 **compartment.** (A) Gating strategy for isolating different Lin⁻HLA-DR⁺ subsets from non-
235 obstructed peritumoral lung resections. Representative flow cytometry plots showing
236 identification of the different DC subsets in human non-obstructed peritumoral lung tissue.
237 Within the viable CD45⁺Lin⁻HLA-DR⁺ cell gate, pDC were identified as CD11c⁻CD123⁺. cDC1
238 were CD16⁻CD11c⁺CD172a⁻CD141⁺ while cDC2 were CD16⁻CD11c⁺CD172a⁺CD1c⁺.
239 Furthermore, CD14⁺ monocytes were CD16⁻CD11c⁺CD172a⁺CD1c⁻CD14⁺ and CD16⁺
240 monocytes were gated as CD16⁺CD11c⁺ cells containing both CD16⁺CD14⁻ and CD16⁺CD14⁺
241 fractions. Finally, a Lin⁻HLA-DR⁺ population was found that scored negative for all markers
242 included in the flow cytometry panel. This population was considered as unidentified (un).
243 Shown are representative dot plots from 3 donors (B) *t*-SNE feature plots of the indicated genes
244 defining expression levels in the different clusters. Each dot represents an individual cell (n=3
245 donors). (C) Flow cytometry analysis of the different DC subsets from non-obstructed
246 peritumoral lung resections revealed a CD14⁺ cDC2 fraction and heterogeneous FcεRI and
247 CD1a expression within cDC2. Shown are representative histograms from 3 donors. (D) Flow
248 cytometry plots depicting expression of FcεRI, CD1a, IRF8 and IRF4 by CD1c⁺CD14⁻ and
249 CD1c⁺CD14⁺ cDC2. Shown are representative plots of 3 non-obstructed peritumoral lung
250 resections.

251

252 **Figure E2: Lung cDC2 are the most potent inducers of Tfh-like cell polarization.** DC
253 subsets were purified from non-obstructed peritumoral lung resections and co-cultured with
254 allogeneic naïve blood CD4⁺ T-cells that were pre-labeled with CFSE. (A) Percentages of
255 ICOS⁺PD-1⁺ T-cells (n=10) in the different DC/T-cell co-cultures were determined at d7 of the

256 co-culture via flow cytometry. Shown are representative flow cytometry plots for the different
257 DC/T-cell co-cultures corresponding to the cumulative data depicted in Figure 2A. (B)
258 Intracellular IL-21 (n=10) and CXCL13 (n=6) staining of ICOS⁺PD-1⁺ (purple), ICOS⁻PD-1⁺
259 (orange), ICOS⁺PD-1⁻ (blue) and ICOS⁻PD-1⁻ (black) T-cell subsets in cDC2/T-cell co-cultures
260 after restimulation with PMA and ionomycin in the presence of Golgi-plug and Golgi-stop.
261 Shown are representative flow cytometry plots corresponding to the cumulative data depicted
262 in Figure 2C (C) Proportions of ICOS⁺CXCR5⁺ T-cells in the different DC/T-cell co-cultures
263 were determined at day 4. Shown are representative flow cytometry plots corresponding to the
264 cumulative data depicted in Figure 2E (n=6). (D) Percentages of PD-1^{hi}BCL6^{hi} cells in
265 ICOS⁺CXCR5⁺, ICOS⁺CXCR5⁻ and ICOS⁻CXCR5⁻ T-cell subsets in the cDC2/T-cell co-
266 cultures were determined via flow cytometry. Shown are representative flow cytometry plots
267 corresponding to the cumulative data depicted in Figure 2F (n=6).

268

269 **Figure E3: Lung cDC2 are the most potent inducers of Tfh-like cell polarization.** DC
270 subsets were purified from non-obstructed peritumoral lung resections and co-cultured with
271 allogeneic naïve blood CD4⁺ T-cells that were prelabeled with CFSE. (A) Proliferation of T-
272 cells was assessed via flow cytometry at day 7. Shown are representative histograms of CFSE^{lo}
273 T-cell proportions present in the indicated co-cultures and combined data graph in which each
274 symbol represents an individual donor (n=10). (B) Intracellular IFN- γ (n=10) staining of
275 ICOS⁺PD-1⁺ (purple), ICOS⁻PD-1⁺ (orange), ICOS⁺PD-1⁻ (blue) and ICOS⁻PD-1⁻ (black) T-
276 cell subsets in cDC2/T-cell co-cultures at day 7 after restimulation with PMA and ionomycin
277 in the presence of Golgi-plug and Golgi-stop. Shown are representative flow cytometry plots
278 and combined data graph in which each symbol represents an individual donor. (C) Percentages
279 of ICOS⁺PD-1⁺IFN- γ ⁺ T-cells in cDC2/T-cell and cDC1/T-cell co-cultures were determined

280 after 7 days. Each symbol represents an individual donor (n=10). **p<0.01, ***p<0.001,
281 Tukey's multiple comparison test (A and B) and Student *t*-test (C).

282

283 **Figure E4: cDC2 from COPD GOLD II lungs display increased potential to promote Tfh-**
284 **like cell skewing.** (A), (B) and (C) cDC2 were isolated from COPD GOLD II peritumoral lung
285 tissues (n=7) and co-cultured with allogeneic naïve CD4⁺ T-cells that were prelabeled with
286 CFSE. Proportions of ICOS⁺PD-1⁺ T-cells (A) and ICOS⁺PD-1⁺IL-21⁺ T-cells (B) were
287 determined at day 7 and compared to cells from non-obstructed peritumoral lung tissues used
288 in Figure 2 (n=10). Shown are representative flow cytometry plots corresponding to the
289 cumulative data depicted in Figure 3A (E4A) and 3B (E4B) respectively. (C) Proliferation of
290 T-cells (% of CFSE^{lo} T-cells) was assessed via flow cytometry at day 7. Shown is combined
291 data graph in which each symbol represents an individual donor. (D) CD1c⁺CD14⁺ fractions
292 within cDC2 from non-obstructed control and COPDII peritumoral lung tissue used in the co-
293 culture experiments presented in Figure 2 and 3. Show is the summary data graph (n=10 for
294 control and n=7 for COPD). (E) Percentages of ICOS⁺PD-1⁺ Tfh-like cells in peritumoral lung
295 tissue resections of COPD and non-obstructed control subjects determined via flow cytometry.
296 Shown are representative flow cytometry plots corresponding to the cumulative data depicted
297 in Figure 3C (n=6 for controls and n=5 for COPD subjects).

298

299 **Figure E5: cDC2 exhibit a unique migratory pattern.** (A) Surface levels of CXCR5, CXCR4
300 and EBI2 were measured on cDC2 and cDC1 from non-obstructed peritumoral lung resections
301 via flow cytometry (n=8 for CXCR5, n=5 for CXCR4 and n=7 for EBI2). Shown are
302 representative flow cytometry histograms for each marker and corresponding isotype.
303 Cumulative data of this experiment depicted in Figure 4A. (B) Surface levels of CXCR5,
304 CXCR4 and EBI2 were measured on cDC2 from non-obstructed and COPD peritumoral lung

305 resections via flow cytometry (control n=8; and COPD n=4 for CXCR5, control n=5; and
306 COPD n=3 for CXCR4 and control n=7; and COPD n=4 for EBI2). Shown is summary data
307 graph for all the markers (mean MFI corrected for background intensity). (C) Surface EBI2
308 levels on ICOS⁺PD-1⁺ (purple), ICOS⁻PD-1⁺ (orange), ICOS⁺PD-1⁻ (blue) and ICOS⁻PD-1⁻
309 (black) T-cell subsets in the lung measured via flow cytometry. Shown are representative flow
310 cytometry histograms for EBI2 and isotype of corresponding cumulative data depicted in Figure
311 4B (n=10).

312 **Supplemental Tables**

313

314 **Table E1: Single Cell cluster markers top 20 by logFC**

Cluster	Gene	avg_logFC
1	FCER1A	2,088139734
1	CD1C	1,706769549
1	CCL17	1,449676397
1	HLA-DQB1	1,198897632
1	CD1E	1,159336889
1	HLA-DQA1	1,084527054
1	FCGR2B	1,068335054
1	CD1A	1,042954992
1	CLEC10A	1,027904208
1	CD1B	0,950553648
1	MS4A6A	0,930901312
1	HLA-DRB1	0,903968868
1	HLA-DRA	0,902474636
1	PKIB	0,890630909
1	CD86	0,829732946
1	C15orf48	0,82015284
1	SGK1	0,81219212
1	MNDA	0,812000223
1	GPR183	0,807344769
1	YWHAH	0,798773794
2	FN1	2,095765876
2	FABP4	1,596997079
2	MARCO	1,563296564
2	GPNMB	1,478726772
2	MSR1	1,390751001
2	MCEMP1	1,37408424
2	MRC1	1,368984707
2	CTSD	1,359952157
2	CCL18	1,351578234
2	FBP1	1,333490303
2	OLR1	1,215738999
2	APOC1	1,121526259
2	CTSB	1,106845823
2	LTA4H	1,067928201
2	LGALS3	1,05322345
2	GCHFR	1,044764711
2	VSIG4	0,960665094
2	CTSL	0,955551603
2	INHBA	0,955106343
2	FTL	0,95059228
3	HBG2	2,302686561
3	HBG1	2,027885733

3	AC104389.5	1,865440664
3	GAGE1	1,610717586
3	GTSF1	1,424267207
3	TOP2A	1,335903152
3	NMU	1,299328361
3	PRAME	1,280435628
3	HBE1	1,274461074
3	HIST1H1C	1,253113637
3	UQCRH	1,252614609
3	CKS1B	1,153736826
3	STMN1	1,131076794
3	PAGE5	1,129167523
3	KRT18	1,105038367
3	XAGE1A	1,088383961
3	TPX2	1,033839997
3	EPRS	1,024921962
3	CENPF	1,021810842
3	IFITM1	1,011736626
4	GZMB	3,575265882
4	JCHAIN	2,767735764
4	PLAC8	2,105195767
4	CCDC50	1,883419665
4	TCF4	1,859471292
4	C12orf75	1,831600843
4	IGKC	1,808955309
4	TCL1A	1,801589347
4	TSPAN13	1,716220583
4	CLEC4C	1,693808536
4	BCL11A	1,674993584
4	IRF4	1,637598991
4	UGCG	1,568753728
4	SELL	1,502616827
4	PPP1R14B	1,47257052
4	SOX4	1,456868998
4	HBB	1,438319472
4	ALOX5AP	1,389828099
4	CLIC3	1,361646152
4	SLC15A4	1,340439327
5	VCAN	1,879909516
5	THBS1	1,710398277
5	S100A8	1,707046345
5	S100A9	1,440827397
5	IL1B	1,339112206
5	EREG	1,241721323
5	FCN1	1,091242627
5	CD300E	1,050490024
5	CXCL8	1,011534339
5	APOBEC3A	0,876431337

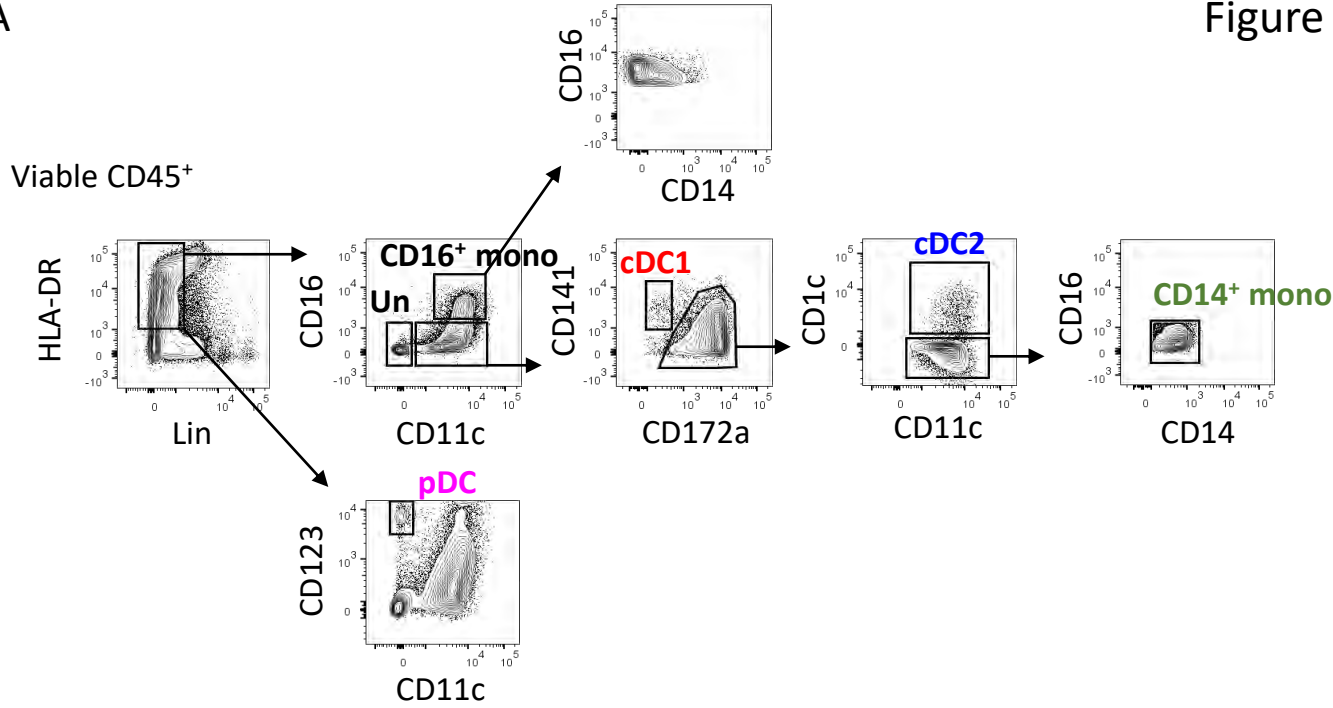
5	SLC11A1	0,84018397
5	BTBD9	0,809890351
5	CNOT11	0,788145477
5	PCDH9	0,753261137
5	LYZ	0,72719212
5	SLC2A3	0,726358945
5	DOCK7	0,725081441
5	RPSAP48	0,719022886
5	AREG	0,716165035
5	NCALD	0,707815369
6	CCL5	3,094512646
6	CD3D	2,545536387
6	CD2	2,251160687
6	TRAC	2,199659021
6	TRBC2	2,065034272
6	CD3G	1,867353038
6	GZMA	1,743103623
6	CD96	1,737923673
6	SYNE2	1,699053241
6	LCK	1,622384641
6	CD52	1,53198628
6	IFNG	1,53013766
6	CLEC2D	1,491061473
6	CD69	1,481444892
6	TRBC1	1,454386996
6	RORA	1,405689794
6	MKI67	1,374739993
6	TNFAIP3	1,301620037
6	TRAT1	1,299873087
6	GNLY	1,295854049
7	FCGR3A	1,721454744
7	FCN1	1,572985976
7	TNFRSF1B	1,285868263
7	LYST	1,271273287
7	MTSS1	1,250671831
7	CTSS	1,235559792
7	SAT1	1,210844606
7	AIF1	1,180556797
7	APOBEC3A	1,117110701
7	LYN	1,090384191
7	COTL1	1,088225378
7	NAMPT	1,066627046
7	MS4A7	1,057457697
7	WARS	1,046454264
7	HCK	0,994740229
7	MAFB	0,95714909
7	CARD16	0,949365146
7	PECAM1	0,920995962

7	POU2F2	0,899423847
7	PSAP	0,899220709
8	C1orf54	2,502920156
8	S100B	2,215423608
8	CPVL	2,05870984
8	WDFY4	2,030191206
8	CPNE3	1,957136877
8	LGALS2	1,665749813
8	SNX3	1,646792957
8	CST3	1,629844392
8	NAPSB	1,60665153
8	IDO1	1,57189014
8	ID2	1,560949215
8	IRF8	1,50888726
8	CLNK	1,473985276
8	CCND1	1,407907195
8	SLAMF7	1,392130385
8	NAAA	1,374342149
8	CLEC9A	1,340110661
8	DNASE1L3	1,339190346
8	RAB7B	1,288662865
8	WFDC21P	1,286948554
9	SCGB3A2	3,795060405
9	SCGB1A1	3,752372645
9	SFTPB	3,513181643
9	SFTPC	3,410659195
9	SLPI	3,237610149
9	BPIFB1	3,006507765
9	SCGB3A1	2,988363079
9	CYB5A	2,353858175
9	PIGR	2,252972921
9	GPRC5A	2,087974649
9	SFTPA1	2,021757317
9	FMO2	1,990456688
9	SFTPA2	1,988487793
9	KRT19	1,877400103
9	FOLR1	1,797672424
9	CXCL17	1,749139084
9	TMC5	1,741303172
9	DNAH5	1,732458055
9	ELF3	1,708781385
9	STEAP4	1,691137143
10	VWF	2,563873467
10	MGP	2,98839516
10	SPARCL1	2,944658372
10	EPAS1	2,867006965
10	IL33	2,614155574
10	TM4SF1	2,581506323

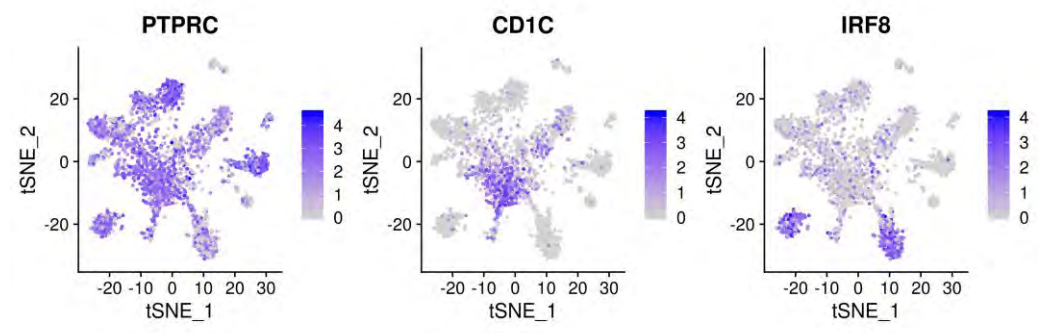
10	CCL21	2,437221467
10	ABI3BP	2,381497238
10	MMRN1	2,356122626
10	ADIRF	2,300596205
10	CAV1	2,290802751
10	PTPRB	2,258068327
10	CTNNAL1	2,252002567
10	CALCRL	2,215405606
10	IGFBP7	2,213770782
10	VCAM1	2,174300302
10	GIMAP7	2,169786669
10	TNFSF10	2,098405801
10	EDN1	2,09597821
10	ADAMTS1	2,082354785
11	CCR7	2,974205214
11	BIRC3	2,682384903
11	LAMP3	2,493221552
11	CCL22	2,414283922
11	TBC1D4	1,811253495
11	IDO1	1,689907394
11	TXN	1,636759411
11	WFDC21P	1,598379937
11	KIF2A	1,572294609
11	DAPP1	1,556414637
11	CCL17	1,522183075
11	NUB1	1,422680026
11	IL7R	1,382598269
11	RASSF4	1,334039962
11	CSF2RA	1,324384725
11	MARCKS	1,322230231
11	CD274	1,307035179
11	C15orf48	1,273655846
11	MARCKSL1	1,269756605
11	BCL2A1	1,267413041
12	CXCL10	3,616408913
12	CCL8	2,755419177
12	GBP1	2,360339823
12	CXCL11	2,235367058
12	CXCL9	2,182283139
12	CCL2	1,808776529
12	C15orf48	1,544114364
12	GBP5	1,497176194
12	IFIT3	1,437316392
12	CALHM6	1,406032207
12	ISG15	1,385695314
12	APOBEC3A	1,376004478
12	STAT1	1,316194086
12	IDO1	1,26595354

12	PLEK	1,180306973
12	LAP3	1,173269394
12	GBP4	1,171045851
12	TFEC	1,025846406
12	ANKRD22	1,023264534
12	SLAMF7	1,021390851
13	HPGDS	3,269991728
13	CPA3	3,249401012
13	MS4A2	3,112447667
13	KIT	2,807435493
13	CD69	2,424658268
13	IL1RL1	2,357782247
13	TPSB2	2,277193757
13	TPSAB1	2,263245984
13	HPGD	2,104334302
13	HDC	2,085005909
13	RHEX	1,992779128
13	SLC18A2	1,987502805
13	RAB27B	1,930387753
13	VWA5A	1,920039685
13	SCGB1A1	1,772399364
13	RGS13	1,772384031
13	PTGS2	1,577393427
13	SLPI	1,501243584
13	ACSL4	1,487190145
13	EGR3	1,472376666
14	FOLR2	2,114128205
14	LYVE1	2,073485389
14	SELENOP	2,056837651
14	SLC40A1	1,998779877
14	RNASE1	1,980077253
14	CXCL3	1,714787741
14	MT1E	1,625695735
14	CD14	1,535402852
14	MT1X	1,51899883
14	CXCL2	1,510258367
14	MT1G	1,468134634
14	F13A1	1,36859711
14	MT2A	1,294103951
14	C3AR1	1,277064909
14	C1QA	1,274293948
14	CD163	1,271227942
14	MSR1	1,269660758
14	CXCL8	1,266401537
14	MAF	1,256446169
14	CCL4	1,238808215

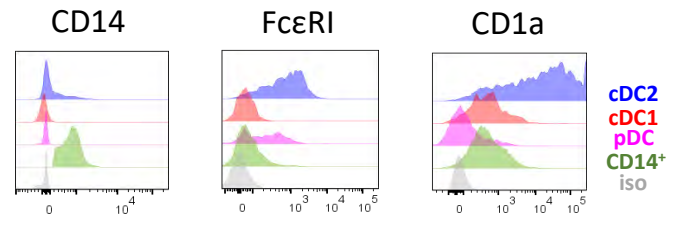
A



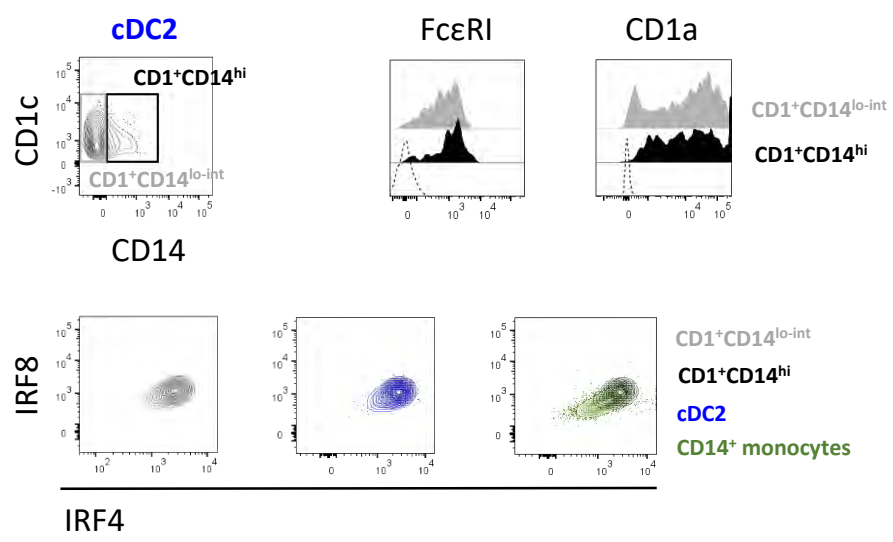
B



C

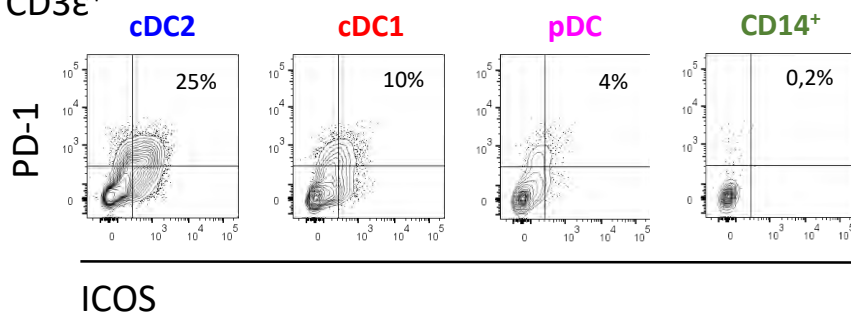


D

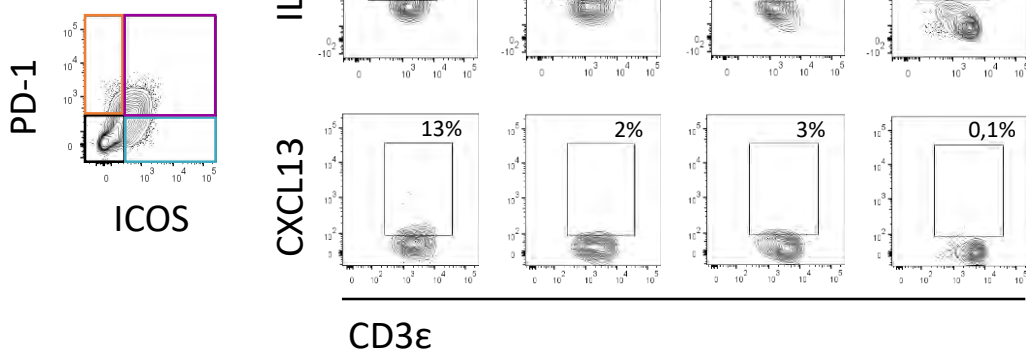


IRF4

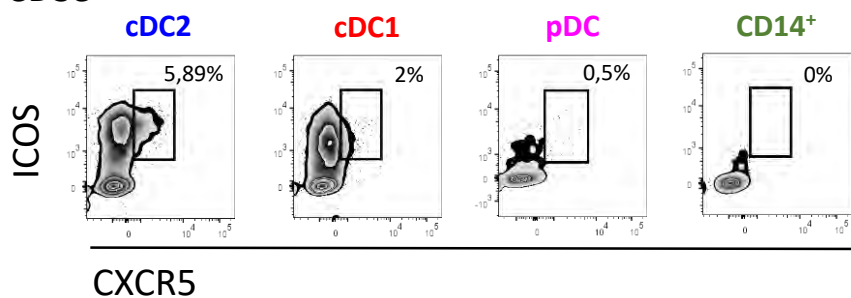
A

Viable CD3 ϵ^+ 

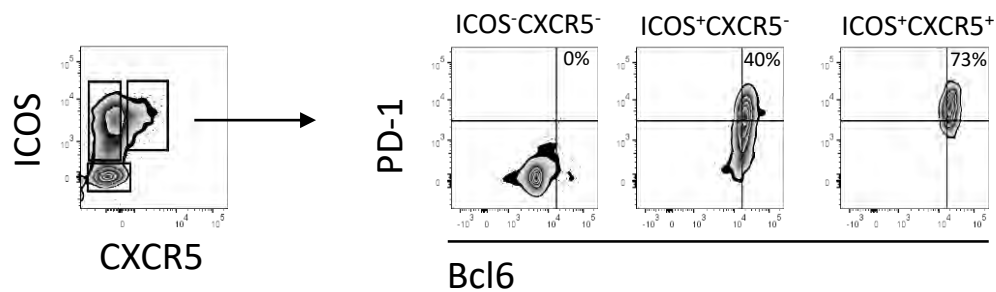
B

Viable CD3 ϵ^+ 

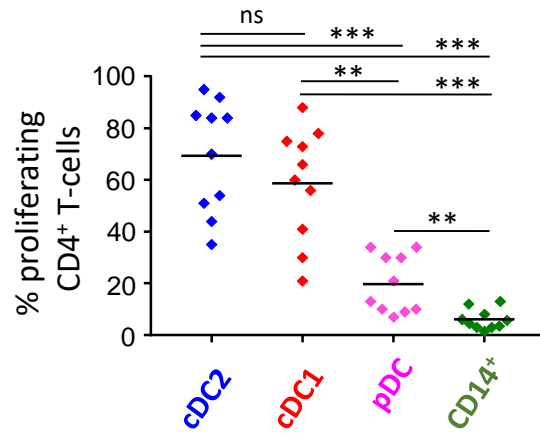
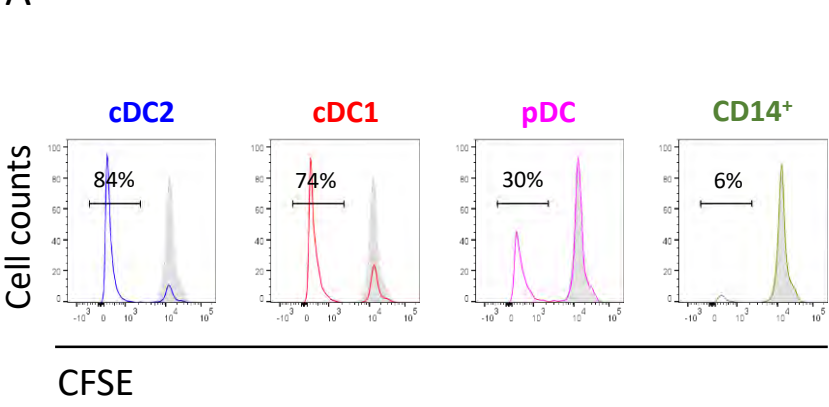
C

Viable CD3 ϵ^+ 

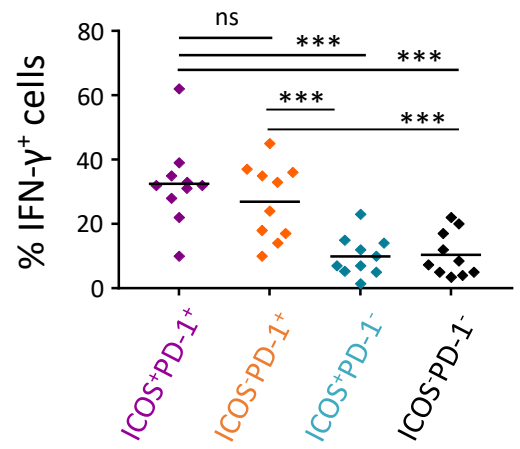
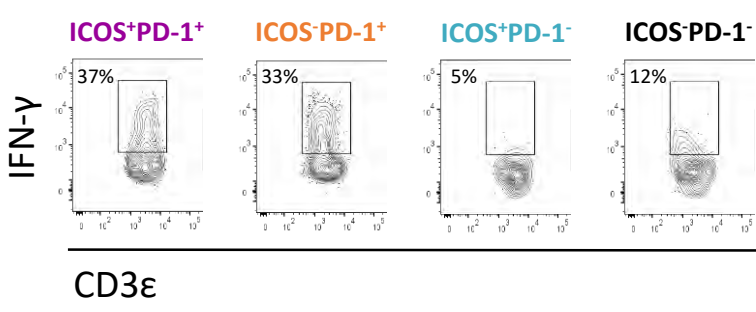
D

Viable CD3 ϵ^+ 

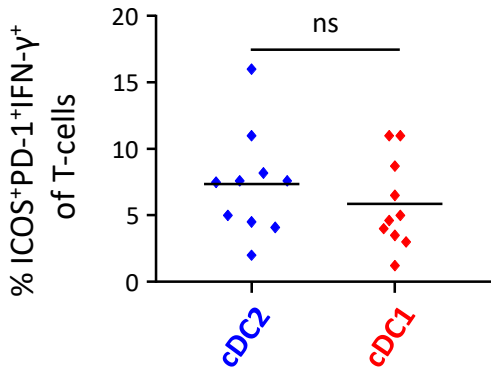
A



B

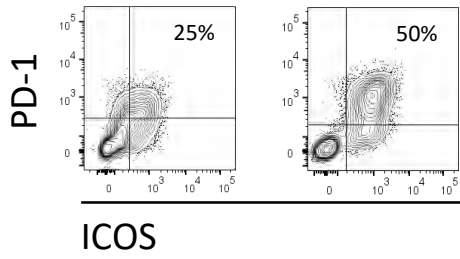


C



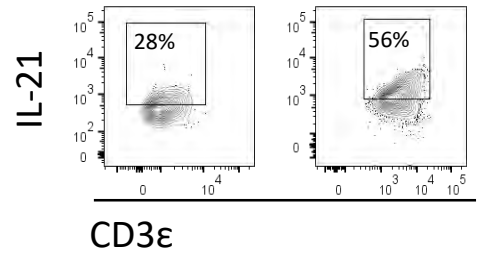
A

Viable CD3ε⁺

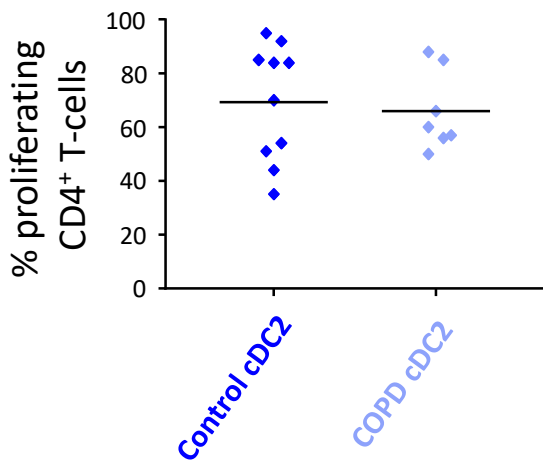


B

Viable CD3ε⁺PD-1⁺ICOS⁺

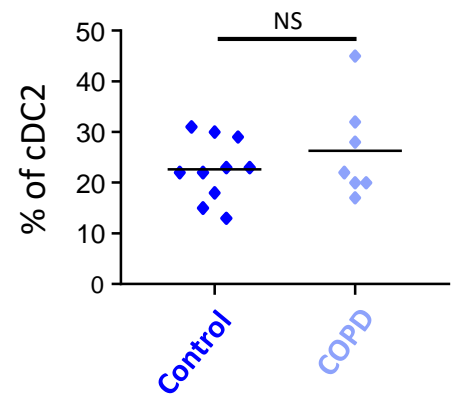


C



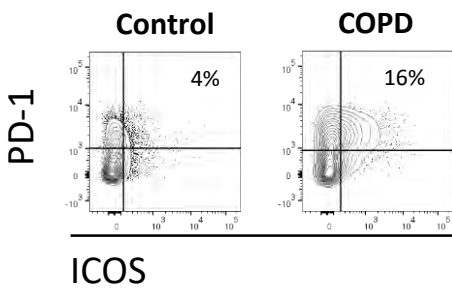
D

CD1c⁺CD14⁺ proportion

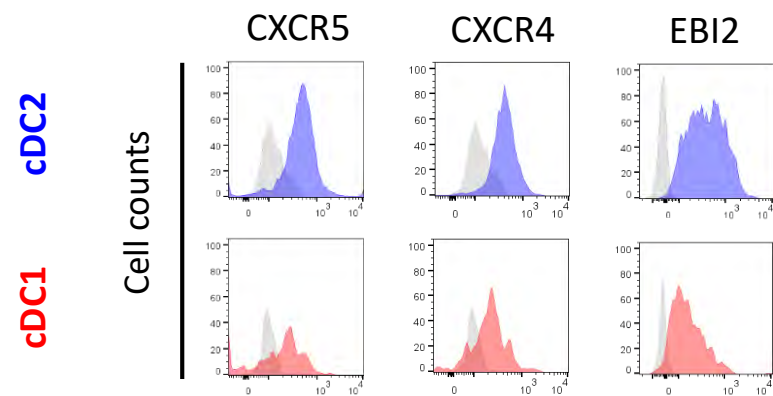


E

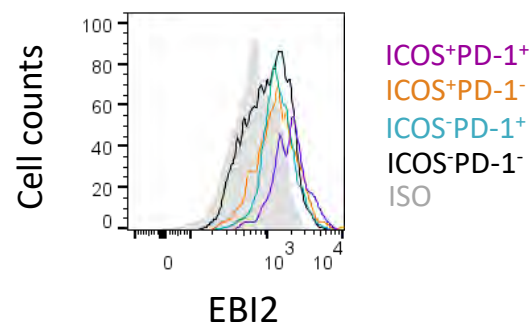
Viable CD3ε⁺ CD4⁺



A



C



B

